

1    **Understanding hydrologic controls of sloping soil  
2    response to precipitation through Machine Learning  
3    analysis applied to synthetic data**

4    Daniel Camilo Roman Quintero<sup>1</sup>, Pasquale Marino<sup>1</sup>, Giovanni  
5    Francesco Santonastaso<sup>1</sup>, Roberto Greco<sup>1</sup>

6    <sup>1</sup>Dipartimento di ingegneria, Università degli Studi della Campania ‘Luigi Vanvitelli’,  
7    via Roma 9, 81031 Aversa (CE), Italy;

8    *Correspondence to:* Daniel Camilo Roman Quintero  
9    (danielcamilo.romanquintero@unicampania.it)

10    **Abstract:**

11    Soil and underground conditions prior to the initiation of rainfall events control  
12    the hydrological processes that occur in slopes, affecting the water exchange  
13    through their boundaries. The present study aims at identifying suitable variables  
14    to be monitored to predict the response of sloping soil to precipitation. The case  
15    of a pyroclastic coarse-grained soil mantle overlaying a karstic bedrock in the  
16    Southern Apennines (Italy) is described. Field monitoring of stream level  
17    recordings, meteorological variables, and soil water content and suction has been  
18    carried out for few years. To enrich the field dataset, a synthetic series of 1000  
19    years has been generated with a physically based model coupled to a stochastic  
20    rainfall model. Machine Learning techniques have been used to unwrap the non-  
21    linear cause-effect relationships linking the variables. The k-means clustering  
22    technique has been used for the identification of seasonally recurrent slope  
23    conditions, in terms of soil moisture and groundwater level, and the Random  
24    Forest technique has been used to assess how the conditions at the onset of  
25    rainfall controlled the attitude of the soil mantle to retain much of the infiltrating  
26    rainwater. The results show that the response in terms of the fraction of rainwater  
27    remaining stored in the soil mantle at the end of rainfall events is controlled by

28 soil moisture and groundwater level prior to the rainfall initiation, giving  
29 evidence of the activation of effective drainage processes.

30 **Keywords:** Water storage, slope response, underground antecedent conditions,  
31 hydrological controls, Random Forest, k-means clustering

32 **1. Introduction**

33 Slope response to precipitation is highly non-linear, in terms of runoff generation,  
34 rainwater infiltration and subsurface drainage processes, which are mostly  
35 depending on the initial soil moisture state at the onset of each rainfall event  
36 (Tromp-Van Meerveld and McDonnell, 2006b; Nieber and Sidle, 2010; Damiano  
37 et al., 2017). The initial (or antecedent) conditions are related to hydrological  
38 processes that occur in the slopes, which control how they exchange water with  
39 the surrounding systems (i.e., atmosphere, surface water, deep groundwater).  
40 These processes occur through the boundaries of the slope, and often evolve over  
41 timescales of weeks or even months, much longer than the duration of rainfall  
42 events, typically ranging between some hours and few days.

43 While the importance of soil moisture conditions on slope runoff and drainage  
44 has been recognized long since (Ponce and Hawkins, 1996; Tromp-Van  
45 Meerveld and McDonnell, 2006a, 2006b), only recently the scientific community  
46 started providing new perspectives to better understand hydrologic conditions  
47 predisposing slopes to landslides (Bogaard and Greco, 2018; Greco et al., 2023),  
48 to explain why most of large rain events do not destabilize slopes, while only  
49 some do (Bogaard and Greco, 2016), and physically based models capable of  
50 integrating hydrological knowledge for predicting landslide occurrence have  
51 been proposed (e.g., Bordoni et al., 2015; Greco et al., 2018; Marino et al., 2021).

52 The triggering of some rainfall-induced geohazards, such as shallow landslides  
53 and debris flows, is favoured by pore pressure increase, caused by rainwater  
54 infiltration and consequent soil moisture accumulation. The storage of rainwater

55 within the soil requires drainage mechanisms developing in the slopes in response  
56 to precipitation to be not so effective to drain out much of the infiltrating water  
57 (Greco et al., 2021; 2023). Consequently, especially for nowcasting and early  
58 warning purposes, the identification of hydrological variables suitable to identify  
59 slope predisposing conditions is extremely useful. Thus, to better understand how  
60 hydrological predisposing conditions may control the processes involving the  
61 sloping soil response in terms of water storage, field monitoring for the  
62 assessment of the slope water balance is highly recommended (Bogaard and  
63 Greco, 2018; Marino et al., 2020a).

64 The identification of suitable variables to be monitored in the field is indeed  
65 useful to achieve an insight of the behaviour of the interconnected hydrological  
66 systems (i.e., groundwater, surface water, soil water). Besides the study  
67 of rainfall-induced landslides, the evaluation of the hydrological scenarios in a  
68 region of interest could impact several other applications, from flood hazard  
69 assessment (Reichenbach et al., 1998; Forestieri et al., 2016; Chitu et al., 2017),  
70 to the prediction of possible crop water stress conditions in relation to defoliation  
71 (Capretti and Battisti, 2007), pathogen expansions in chestnut grove (Gao and  
72 Shain, 1995), and plant mortality in a climate change context (McDowell et al.,  
73 2008).

74 This research focuses on a case study of a slope located in Campania (southern  
75 Italy), representative of a wide area frequently hit by destructive rainfall-  
76 triggered shallow landslides (e.g., Fiorillo et al., 2001; Revellino et al., 2013). In  
77 fact, such geohazards are recurrent along the carbonate slopes covered with  
78 unsaturated air-fall pyroclastic deposits, diffuse over an area of few thousand  
79 square kilometres around the two major volcanic complexes of the region, the  
80 Somma-Vesuvius and the Phlaegrean Fields (Di Crescenzo and Santo, 2005;  
81 Cascini et al., 2008). The underlying limestone bedrock, densely fractured, is  
82 characterised by the presence of deep karst aquifers (Allocca et al., 2014). The

83 triggering mechanism of landslides in the area is the increase of water storage  
84 within the soil mantle after intense and persistent precipitation, leading to pore  
85 pressure build up (Bogaard and Greco 2016). Slope equilibrium is in fact  
86 guaranteed by the additional shear strength promoted by soil suction (Lu and  
87 Likos 2006; Greco and Gargano 2015), which reduction often leads to slope  
88 failure due to shear strength loss by soil wetting during rainwater infiltration  
89 (Olivares and Picarelli, 2003; Damiano and Olivares, 2010; Pagano et al., 2010;  
90 Pirone et al., 2015).

91 Recent studies show that the response of the soil mantle to precipitation in the  
92 study area is affected not only by rainfall characteristics and antecedent soil  
93 moisture, but also by the wetness of the interface with the underlying bedrock,  
94 which controls the leakage of water into the underlying fractured limestone  
95 (Marino et al., 2020a; 2021). At the contact between soil and bedrock, intense  
96 weathering modifies the physical properties of the soil as well as of the fractured  
97 bedrock, which form a hydraulically interconnected system, the epikarst (e.g.,  
98 Perrin et al., 2003; Hartmann et al., 2014; Dal Soglio et al., 2020). The changing  
99 hydraulic behaviour of the soil-bedrock interface can be related to the storage of  
100 water in the epikarst, where a perched aquifer forms during the rainy season  
101 (Greco et al., 2014, 2018).

102 The aim of this study is to identify the major hydrological processes controlling  
103 the response to precipitation of the pyroclastic soil mantles typical of the area,  
104 and the seasonally recurrent conditions that affect their attitude to retain much of  
105 the infiltrating rainwater, through suitable measurable variables. To this aim, a  
106 rich dataset of measured rainfall events and corresponding hydrological effects  
107 would be required, which was not available for the case study, where monitoring  
108 activities had been carried out for few years. Therefore, a synthetic 1000 years  
109 hourly dataset was generated, by means of a stochastic rainfall model and a  
110 simplified physically based model of the slope, coupling the unsaturated

111 pyroclastic soil mantle and the underlying perched aquifer (Greco et al., 2018).  
112 Both models had been previously calibrated and validated on field experimental  
113 data (Damiano et al, 2012; Greco et al., 2013; Comegna et al., 2016; Marino et  
114 al., 2021). The synthetic data of soil suction, water content and aquifer water  
115 level, all measurable in the field and assumed as representative of real conditions,  
116 were analysed as if they were measured data. After sorting the rainfall events  
117 within the 1000 years timeseries, a dataset was built with the antecedent  
118 conditions one hour before the beginning of each rainfall event. It included the  
119 previously listed variables plus the total event rainfall depth, and the change in  
120 the water stored in the soil mantle at the end of each rainfall event. To disentangle  
121 the non-linear processes controlling the hydraulic behaviour of the slope, and  
122 their role on the soil response to precipitation, the dataset was analysed with  
123 Machine Learning (ML) techniques, i.e., clustering, and random forest. Indeed,  
124 ML allows managing big amounts of data, such as those provided by assimilation  
125 of extensive monitoring networks, remote sensing, satellite products and other  
126 sources, without introducing any mathematical model structure to highlight the  
127 cause-effect relationships linking the variables.

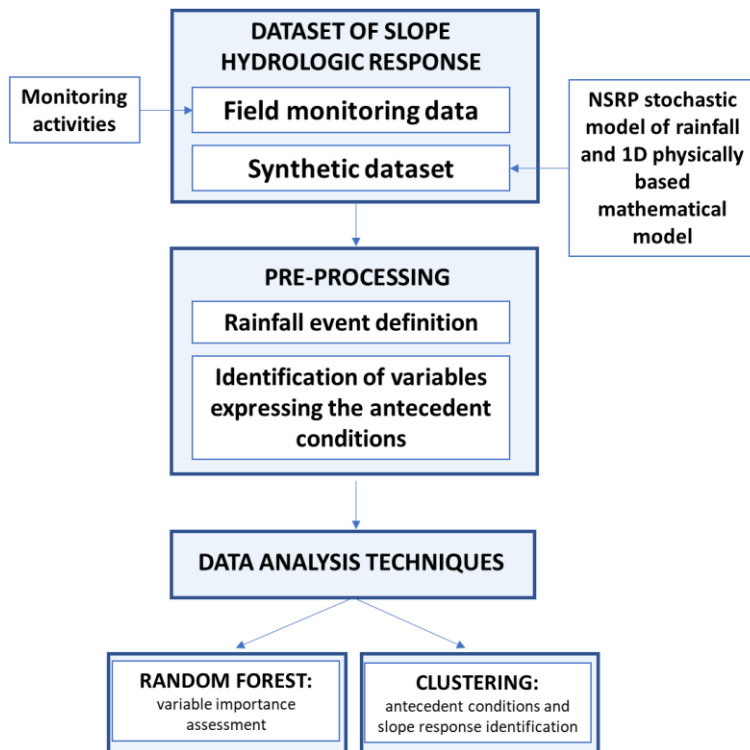
128

129        **2. Materials and methods**

130        The studied slope, described in section 2.1, belongs to the Partenio Massif, and it  
131        has the typical characteristics of many pyroclastic slopes of Campania (southern  
132        Italy) (Greco et al., 2018). Indeed, three major zones characterized by unsaturated  
133        pyroclastic deposits can be identified in Campania (Cascini et al., 2008):  
134        Campanian Apennine chain, composed by carbonate rock covered by a variable  
135        layer of pyroclastic soil (from 0.1 to 5 m); Phlegraean district, formed by  
136        underlying densely fractured volcanic tuff bedrock, placed under several meters  
137        of pyroclastic soils; and Sarno and Picentini Mountains, where a thin layer of  
138        pyroclastic material is over a terrigenous bedrock. In these three areas, the  
139        thickness of the soil mantle is quite variable, according to the slope inclination  
140        and to the distance from the eruptive centre (De Vita et al., 2006; Tufano et al.,  
141        2021).

142        To identify the seasonally recurrent conditions that affect the attitude of the soil  
143        mantle to retain much of the infiltrating water, a large set of measurements of  
144        rainfall events, and their effects on the slope, would be required. Hence, to enrich  
145        the data available from the monitoring activities carried out for some years at the  
146        slope (Marino et al., 2020a), a synthetic dataset of the hydrologic response of the  
147        slope to precipitation, has been generated with a NSRP stochastic model of  
148        rainfall (Rodriguez-Iturbe et al., 1987) and a simplified 1D model of the  
149        interaction of the unsaturated pyroclastic soil mantle with the underlying perched  
150        aquifer forming in the epikarst. Both the models, described in the following  
151        sections, had been previously developed based on experimental data (Greco et  
152        al., 2013; 2018; Marino et al., 2021). The obtained synthetic dataset has been  
153        compared to the limited dataset from field monitoring, showing a reasonable  
154        agreement. Therefore, it has been considered suitable to reproduce slope response  
155        to climate forcing, in terms of soil volumetric water content and perched aquifer  
156        water level, in the studied area (see Section 2.2).

157 The synthetic dataset has been analysed with Machine Learning techniques  
158 (Section 2.3), as they result quite powerful to identify non-linear cause-effect  
159 relationships between variables, without introducing any model structure, as if  
160 the data were provided by field measurements. Figure 1 shows the flowchart of  
161 the entire methodology.

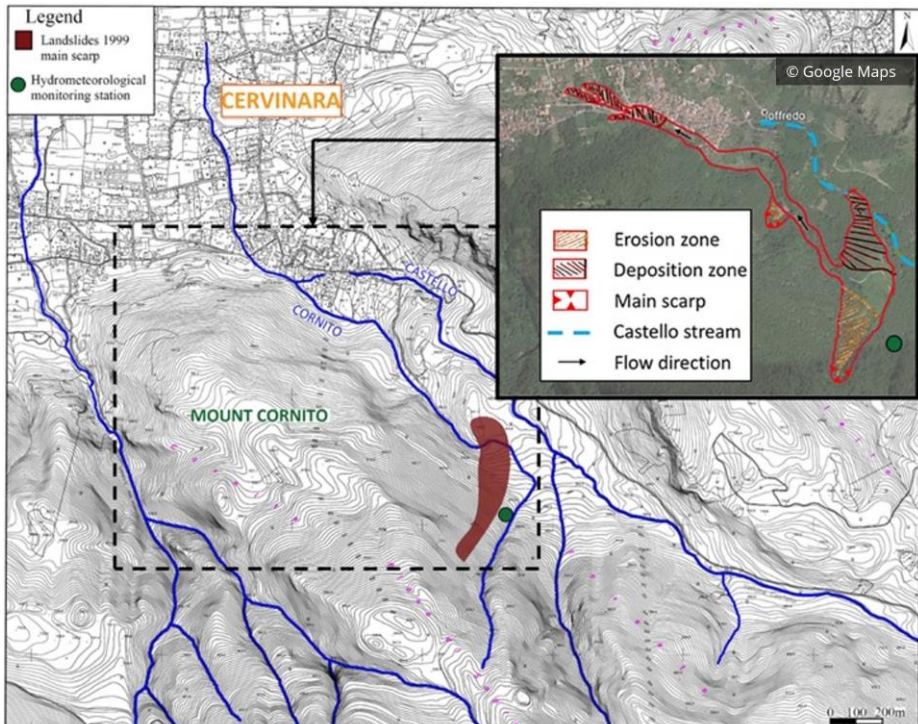


162  
163 **Figure 1. Flowchart summarizing the methodology followed in the analysis**  
164 **of sloping soil response to precipitation.**

## 165       **2.1. Case study**

166 The study area refers to the north-east slope of Monte Cornito, part of the Partenio  
167 Massif (Campania, southern Italy), 2 km from the town of Cervinara, about 40  
168 km northeast of the city of Naples. The slope was involved in a series of rapid  
169 shallow landslides after a rainfall event of 325 mm in 48 hours during the night  
170 between 15–16 December 1999, causing casualties and heavy damages (Fiorillo  
171 et al., 2001). A field monitoring station was installed nearby the big landslide

172 scarp since 2001. Further details of the investigated zone, with indications of the  
173 area affected by the largest of the landslides triggered in 1999, are shown in  
174 Figure 2.



175  
176 **Figure 2. Location of the study area and indication of the zone affected by a large**  
177 **landslide in 1999. Adapted from: Marino et al. (2020a).**

178 Partenio Massif is part of the southern Apennines area. The bedrock mainly  
179 consists of Mesozoic-Cenozoic fractured limestones, mantled by loose  
180 pyroclastic deposits, resulting from the explosive volcanic activity of Somma-  
181 Vesuvius and Phleorean Fields, which occurred over the last 40.000 years  
182 (Rolandi et al., 2003).

183 The fractured limestone formations of the southern Apennines often host large  
184 karst aquifers, through which a basal groundwater circulation occurs, for which  
185 regional groundwater recharge between 100 and 500 mm/year has been  
186 estimated, with 200 mm/year regarding the area of Cervinara (Allocca et al.,

187 2014). Moreover, recent studies showed that, in the upper part of the karst system,  
188 denoted as epikarst (Hartmann et al., 2014), more permeable and porous than the  
189 underlying rock, a perched aquifer often develops (Williams, 2008; Celico et al.,  
190 2010). It temporally stores water and favors the recharge of the deep aquifer  
191 through the larger fracture system. The water, which is accumulated temporally  
192 in the epikarst, also reappears at the surface in small ephemeral streams.

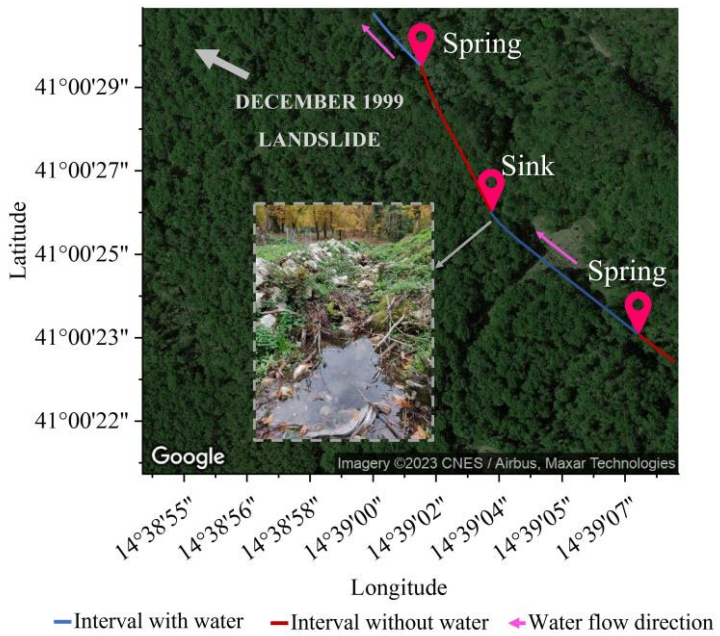
193 Specifically, the slope of Cervinara has an inclination between 35° and 50°, at an  
194 elevation between 500 m and 1200 m above sea level. The soil mantle, usually  
195 in unsaturated conditions, is the result of the air-fall deposition of the materials  
196 from several eruptions, so it is generally layered. It mainly consists of layers of  
197 volcanic ashes (with particle size in the range of sands to loamy sands) alternating  
198 with pumices (sandy gravels), laying upon the densely fractured limestone  
199 bedrock. Near the soil-bedrock interface, a layer of weathered ashes,  
200 characterized by finer texture (silty sand), with lower hydraulic conductivity,  
201 moderate plasticity and low cohesion, is often observed (Damiano et al., 2012).

202 The soil mantle thickness varies spatially from a minimum of 1.0 m, in the  
203 steepest part of the slope, to larger values at its foot (up to 4-5 meters). The thin  
204 soil mantle, compared to the slope width and length of hundreds of meters (Figure  
205 2), makes the flow processes nearly one-dimensional, except for the close  
206 proximity to geometric singularities.

207 The pyroclastic soils of the profile are characterized by high porosity (from about  
208 50% for the pumices, to 75% for the ashes) and quite high values of saturated  
209 hydraulic conductivity (ranging up to the order of  $10^{-5}$  m/s). Thus, this kind of  
210 soil lets rainwater infiltrate even during the most intense rainfall events, with little  
211 runoff generation, and it can store a large amount of water without approaching  
212 saturation. The values of soil capillary potential, measured during the rainy

213 season, rarely exceed -0.5 m, as observed also in other slopes of the area (Cascini  
214 et al., 2014; Comegna et al., 2016; Napolitano et al., 2016).

215 The climate is Mediterranean, which is characterized by dry and warm summer  
216 and rainy autumn and winter, with mean annual precipitation of about 1600 mm,  
217 mostly occurring between October and April. The total potential  
218 evapotranspiration ET<sub>0</sub>, estimated with the Thornthwaite formula (Shuttleworth,  
219 1993), is between 700 mm and 800 mm in the altitude range between 750 m and  
220 400 m (Greco et al., 2018). The vegetation mainly consists of widespread  
221 deciduous chestnuts, with a dense understory of brushes and ferns, growing  
222 during the flourishing period (between May and September). In fact, visual  
223 inspections of the soil profile showed a large amount of organic matter and roots.  
224 In most cases, roots are denser in the uppermost part of the soil mantle and  
225 become sparse between the depth of 1.50 m and 2.00 m below the ground surface,  
226 reaching the basal limestones and penetrating the fractures.



227  
228 **Figure 3. Identification of surface water flow in the Castello stream at the beginning**  
229 **of the rainy season in November 2021 by visual recognition of springs and sinks in**  
230 **the watercourse**

Moreover, in the surrounding area, several ephemeral and perennial springs are present, mostly located at the foot of the slopes, which supply a network of small creeks and streams, allowing to show the activity of the aquifer discharge to the surface water. An indication regarding the Castello stream (the main stream for this side of the basin), with springs, is shown in Figure 3, where, during a field recognition in November 11<sup>th</sup> 2021, the surface water flow appeared (springs) and disappeared (sinks) in some points along the stream course. Normally the stream exhibits its lowest water depth values up to the beginning of the late autumn (Marino et al., 2020a, p.3.3), but it is interesting to note that the surface water in the stream emerging from the epikarstic springs is an indicator of the active slope drainage.

### **2.1.1. Field monitoring data**

Several hydrological monitoring activities have been carried out at the slope of Cervinara since 2001, initially consisting of measurements of precipitation and manual readings (every two weeks) of soil suction by “Jet-fill” tensiometers, equipped with a Bourdon manometer (Damiano et al., 2012). Afterwards, since November 2009, an automatic monitoring station has been set at an elevation of 585 m a.s.l., near a narrow track close to the landslide scarp of December 1999. The installed instrumentation consisted of tensiometers, time domain reflectometry (TDR) probes for water content measurements, and a rain gauge (Greco et al., 2013; Comegna et al., 2016).

Since 2017, the hydro-meteorological monitoring was enriched (Marino et al., 2020a), aiming at understanding the seasonal behaviour of the slope and the interactions between the hydrological systems, i.e., the unsaturated soil mantle, the epikarst, and the underlying fractured bedrock.

Specifically, the data collected by tensiometers and TDR probes were supplemented with those from a meteorological station (composed by a thermo-

258 hygrometer, a pyranometer, an anemometer, a thermocouple for soil temperature  
259 measurement, and a rain gauge), and with the water level in two streams at slope  
260 foot, so to gain useful information for the assessment of the water balance of the  
261 studied slope.

262 The data from field monitoring, carried out between 2017 and 2020 with hourly  
263 resolution, consist of rainfall, evapotranspiration, soil moisture and suction at  
264 various depths, and the water depth of the Castello stream. The data have been  
265 useful to highlight seasonally recurrent soil moisture distributions. More details  
266 about the measured data and the observed recurrent seasonal behaviour of the  
267 area of Cervinara can be found in Marino et al. (2020a).

268       **2.2. Synthetic dataset**

269 Aiming at identifying suitable variables to be monitored in the field for the  
270 identification of the conditions controlling different slope responses to the  
271 precipitation, a rich dataset of rainfall and underground monitored variables, such  
272 as soil moisture and groundwater level, is needed. However, a complete field  
273 monitored dataset is not always possible to be analyzed and, when it exists, it is  
274 commonly available for short periods, granting a relatively small number of  
275 measurements. Hence, a synthetic dataset, aiming at improving the information  
276 obtained from field monitoring, has been generated. This dataset has been  
277 obtained by means of the physically based mathematical model described  
278 hereinafter (section 2.2.2). The model has been run with a 1000 years synthetic  
279 hourly rainfall series, obtained with a stochastic rainfall generator, for which  
280 further details are given in section 2.2.1. The choice of such a long synthetic  
281 series has been made to obtain an amount of data, representative also of  
282 conditions rarely occurring at the slope, large enough to ensure significance of  
283 the analyses carried out with ML techniques. In this respect, it is worth noting  
284 that the adopted clustering and Random Forest techniques allow easily handling  
285 big amounts of data without unaffordable computational burden.

286        **2.2.1. Definition of synthetic rainfall events**

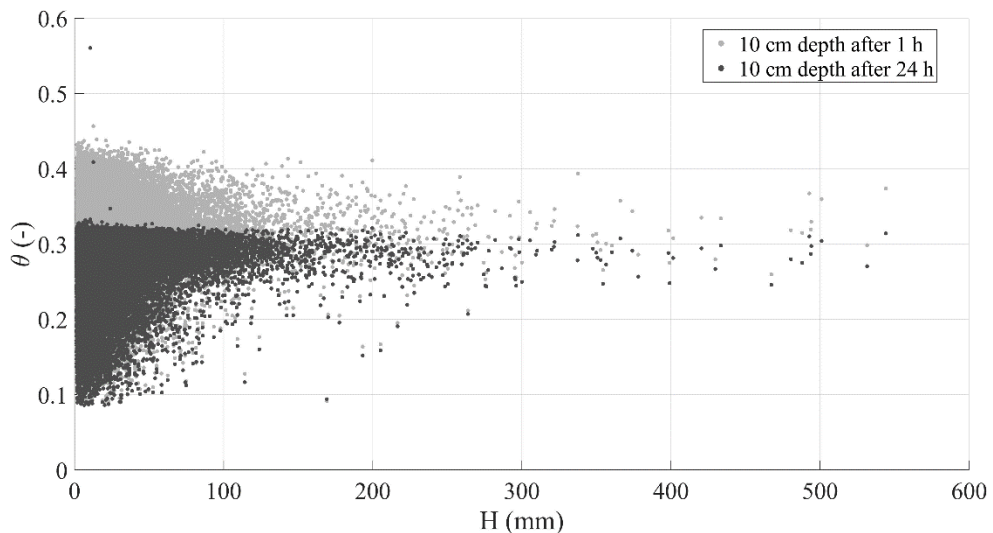
287        The Neyman-Scott rectangular pulse model (NSRP) has been used to obtain a  
288        1000 years long synthetic hourly series of precipitation. The NSRP model  
289        reproduces the precipitation process as a set of rain clusters, composed by  
290        possibly overlapping rain cells embodied by rectangular pulses, each one with  
291        random origin. The storm duration is represented by the cell width and its height  
292        represents the associated rainfall intensity, so that when multiple cells overlap,  
293        the total intensity is the sum of the intensities of the overlapping cells (Rodriguez-  
294        Iturbe et al. 1987; Cowpertwait et al. 1996).

295        NSRP model calibration requires the identification of five parameters, using the  
296        method of moments (Peres and Cancelliere, 2014), based on available rainfall  
297        data for the investigated site. Specifically, the data from the rain gauge station of  
298        Cervinara, situated near the Loffredo village, belonging to the Civil Protection  
299        Agency of Campania Region available from January 2001 to December 2017  
300        with a time resolution of 10 min, were used.

301        The aim of this study is the identification of variables expressing the slope  
302        conditions responsible of different responses to precipitation. In that sense, it is  
303        important to define the events within the rainfall time series to clearly distinguish  
304        antecedent conditions from the effects of the current rainfall event.

305        In other words, within the 1000 years long time series, a criterion should be  
306        identified to separate rainfall events, so that a new event begins only when the  
307        effects of the previous one disappeared. For this study, the events were defined  
308        as periods with at least 2mm of rainfall, preceded and followed by at least 24h  
309        with less than 2mm (i.e., smaller than the mean daily potential evapotranspiration  
310        estimated for the case study). Indeed, the separation period of 24 hours is  
311        commonly used for the definition of the empirical thresholds for early warning

312 systems against rainfall-induced landslides (e.g., Peres et al., 2018; Segoni et al.,  
313 2018, Marino et al., 2020b).



314

315 **Figure 4. Scatter plot of event rainfall depth and mean volumetric water content of**  
316 **the top 10 cm soil depth 1 hour (grey dots) and 24 hours (black dots) after the end**  
317 **of each rainfall event**

318 In fact, the mean volumetric water content ( $\theta$ ) at 10 cm depth drops below soil  
319 field capacity ( $\theta \approx 0.35$ ) 24 hours after the end of each event (Figure 4) in all  
320 the cases in which such value was overcome before the end of the event. This  
321 shows that a dry interval of 24 hours after a rainfall event is long enough for  
322 drainage processes to remove from the topsoil most of the water infiltrated from  
323 the previous event. As topsoil moisture controls the infiltration capacity at ground  
324 surface, after such interval the infiltration of new rainfall is only little affected by  
325 the remnants of the previous rainfall event.

326 With the assumed separation criterion, a total of 53061 rainfall events within  
327 1000 years are obtained, with durations ranging between 1 and 570 hours, and  
328 total rainfall depth between 2 and 710 mm.

329        **2.2.2. Slope hydrological model**

330        As already pointed out in Section 2.1, the regular geometry of the slope, and the  
331        hydraulic characteristics of the soils, make the flow processes in the soil mantle  
332        mostly one-dimensional. Indeed, a simplified 1-D model had been previously  
333        developed and successfully validated according to the data collected during the  
334        hydrological monitoring activities (Greco et al., 2013; Greco et al., 2018), and  
335        was applied to investigate the hydrological response of the slope to synthetic  
336        hourly precipitation data. The unsaturated flow through the soil mantle is  
337        modelled with 1-D head-based Richards' equation (Richards, 1931), assuming  
338        for simplicity a single homogeneous soil layer, and it is coupled with a model of  
339        the saturated water accumulated in the perched aquifer. The adoption of a 1-D  
340        model is allowed thanks to the geometry of the considered mantle, as well as to  
341        the prevailing water potential gradients orthogonal to the ground surface when  
342        the soil is in unsaturated conditions.

343        The root water uptake has been accounted in the source term of the model,  
344        according to the expressions by Feddes et al. (1976), based on estimated potential  
345        evapotranspiration, with maximum root penetration depth equal to the soil mantle  
346        thickness and triangular root density shape.

347        Two boundary conditions are considered for the unsaturated soil mantle. At  
348        ground surface (i.e., the upper boundary condition), if the rainfall intensity is  
349        greater than the current infiltration capacity, the excess rainfall forms overland  
350        runoff. Otherwise, all rainfall intensity is set as infiltration. The bottom boundary  
351        condition links the soil mantle to a perched aquifer developing in the fractures  
352        and hydraulically connected to the unsaturated cover through the weathered soil  
353        layer (less conductive and capable of retaining much water), located at the contact  
354        between the cover and the bedrock. This soil layer penetrates the vertical conduits  
355        and fractures (Greco et al., 2013). In this context, the perched aquifer is modelled  
356        as a linear reservoir model, that receives water from the gravitational leakage of

357 the overlying unsaturated soil mantle and releases it as deep groundwater  
358 recharge and spring discharge (Greco et al., 2018). This conceptualization of the  
359 perched aquifer behaviour implies that the streamflow, supplied by the springs,  
360 is linearly related to the aquifer water level temporarily developing in the  
361 epikarst. Indeed, with this assumption, the model closely reproduces the trend of  
362 the stream water level observed in the field (Greco et al., 2018; Marino et al.,  
363 2020a). The pressure head at the soil–bedrock interface is assumed to follow the  
364 fluctuations of the water table of the underlying aquifer.

365 The hydraulic parameters of the homogeneous soil mantle have been obtained  
366 considering the information from previous laboratory tests (Damiano and  
367 Olivares, 2010) and field monitoring data analysis (Greco et al., 2013),  
368 considering the van Genuchten-Mualem model for the hydraulic characteristic  
369 curves (van Genuchten, 1980). Specifically, the parameters of the hydraulic  
370 characteristic curves were searched with a Genetic Algorithm, constrained within  
371 intervals ensuring the obtained curves to resemble available measurements of  
372 water retention and unsaturated hydraulic conductivity, obtained both in the field  
373 and in the laboratory (Greco et al., 2013). The parameters describing the  
374 hydraulic behaviour of the perched aquifer hosted in the upper part of the  
375 limestone bedrock have been derived from previous studies, which showed that  
376 the model satisfactorily reproduced the fluctuations of water potential and  
377 moisture, observed at various depths in the unsaturated soil cover, both during  
378 rainy and dry seasons (Greco et al., 2013; 2018). Model parameters are  
379 summarized in Table 1. The groundwater level of the perched aquifer is referred  
380 to the base of the epikarst, which is assumed 14 m below the soil-bedrock  
381 interface.

382

383      **Table 1. Hydraulic parameters of the coupled model of the unsaturated soil mantle**  
 384      **and of the aquifer hosted in the epikarst** (Greco et al. 2021).

	Soil mantle thickness (m)	2
	Saturated water content (-)	0.75
	Residual water content (-)	0.01
Soil mantle	Air entry value ( $m^{-1}$ )	6
	Shape parameter (-)	1.3
	Saturated hydraulic conductivity (m/s)	$3 \times 10^{-5}$
	Epikarst thickness (m)	14
Epikarst	Effective porosity (-)	0.005
	Time constant of linear reservoir (days)	871 days

385  
 386      The equations have been numerically integrated with the finite difference  
 387      technique, with a time step of 1 hour over a spatial grid with vertical spacing of  
 388      0.02 m.

389      The model assumes a homogeneous soil profile and a simplified slope geometry,  
 390      and indeed it is not aimed at reproducing the details of flow processes through  
 391      the unsaturated soil mantle. Consequently, the hydraulic properties of the  
 392      homogeneous soil layer should be considered as effective properties, useful to  
 393      reproduce the major features of the infiltration and drainage phenomena. The  
 394      model is rather used to assess how large-scale (in time and space) hydrological  
 395      processes, such as long-term cumulated rainfall and evapotranspiration and  
 396      perched aquifer recharge, control the conditions that affect the response of the  
 397      soil mantle to precipitation events. In this sense, the obtained results can be  
 398      considered representative for large areas that share the major geomorphological  
 399      features of the slopes of Partenio Massif.

400      **2.2.3. Synthetic hydrometeorological data**

401      As it has been stated from previous sections, the dataset comes from the  
 402      simulation of the hydrologic response of a slope to 1000 years long hourly rainfall  
 403      time series, carried out with a physically based model, calibrated for the case

404 study. The output contains the time series of soil water content and suction at all  
405 depths throughout the soil mantle, of the water exchanged between the soil and  
406 the atmosphere, of the leakage through the soil-bedrock interface, and of the  
407 predicted water level of the underlying aquifer.

408 One hour before the onset of each rainfall event, the following variables have  
409 been extracted, as they would be measurable in the field and are representative  
410 of antecedent conditions: the aquifer water level ( $h_a$ ), the mean volumetric water  
411 content in the uppermost 6 cm of soil mantle ( $\theta_6$ ) and the mean volumetric water  
412 content in the uppermost 100 cm of soil mantle ( $\theta_{100}$ ). To quantify the effects of  
413 rainfall on the slope response, the change of the water stored in the soil mantle at  
414 the end of each rainfall event ( $\Delta S$ ) has been computed and compared with the  
415 total rainfall depth of the event (H).

416 Specifically, the inclusion of soil water content information has been chosen, as  
417 it can be obtained from available satellite-derived remote sensing products  
418 (Paulik et al., 2014; Pan et al., 2020) or from field sensor networks (Wicki et al.,  
419 2020). Regarding satellite products, in many cases not giving precise water  
420 content values, they satisfactorily reproduce temporal trends, which represent a  
421 valuable information for hazard assessment.

422 Besides, as the model introduces a linear relationship to estimate the outflow  
423 from the groundwater system, the monitored stream water level has been  
424 considered interchangeable with the simulated groundwater level, as the two  
425 variables are assumed directly linked in the model.

### 426      **2.3. Data analysis techniques**

427 The resulting dataset has been analyzed with Machine Learning techniques,  
428 aiming at capturing the complex interactions between the hydrological  
429 subsystems (i.e., soil mantle, fractured bedrock, surface water). Indeed, the  
430 analysis of the data is not only constrained to classical statistical analyses, such

431 as data frequency distributions, but also to data classification based on their  
432 geometrical distribution, and on quantifying the importance of the considered  
433 antecedent variables on the simulated response as well.

434 **2.3.1. Variable importance assessment by Random Forest**

435 Aim of this study is to find a set of measurable variables which, based only on  
436 field measurements, provide valuable information for predicting the response of  
437 the soil mantle to precipitation. In this respect, a suitable tool is represented by  
438 Random Forest (RF), a Machine Learning method that sets its basis on the theory  
439 of regression/classification trees, bagging data and capturing even the complex  
440 or non-linear interactions in-between the data of a set with relatively low bias  
441 (Breiman, 2001). This method is often used to forecast a desired variable based  
442 on predictor variables in terms of regression or classification set of randomly  
443 constructed trees. RF analysis of importance allows quantifying how informative  
444 the input variables are to make good predictions of the output, which should not  
445 be confused with the information provided by a variance-based Sensitivity  
446 Analysis (SA). In fact, this latter, always based on a mathematical model linking  
447 input variables to output, explains how the variability of the output is related to  
448 the variability of the inputs, regardless how the output of a model resembles  
449 available observations. As in this case the analysed data set is synthetic, i.e., it  
450 has been obtained through a mathematical model, the results of a variance-based  
451 SA will also be presented, allowing to compare the different kind of information  
452 provided by the two analyses.

453 In this case, a regression based Random Forest technique is applied to predict the  
454 soil storage response ( $\Delta S$ ) at the end of each rainfall event of total depth  $H$ , using  
455 as predictors all possible triplets of variables described in the section 2.2.3 ( $H$ ,  
456  $h_a$ ,  $\theta_6$  and  $\theta_{100}$ ). Specifically, four Random Forest models have been developed:  
457 RF1 with input features  $\langle H, \theta_6, h_a \rangle$ , RF2, with input features  $\langle H, \theta_{100}, h_a \rangle$ , RF3,  
458 with as input features  $\langle H, \theta_6, \theta_{100} \rangle$  and RF4 with input features:  $\langle H, \theta_6, \theta_{100} \rangle$ . The

459 80% of the dataset was used to train the models and tuning the major  
460 hyperparameters of random forest algorithm: the number of trees, the maximum  
461 depth, the minimum sample leaf, and the maximum number of feature (more  
462 details about the evaluation and optimization of the hyperparameters are provided  
463 in Appendix B).

464 Then, the best predictor triplet of variables is selected according to the lowest  
465 value of the Root Mean Squared Error (RMSE) calculated using the test data set  
466 consisting of the 20% of the remaining data.

467 Furthermore, to understand how a single predictor variable affects the regression  
468 model, the importance of input variables (features) in the Random Forest  
469 regression model has been assessed through the mean decrease in impurity  
470 (Breiman, 2001), which is a measure of the ability of the tree to split the dataset  
471 in classes. Impurity is here computed as the mean decrease of RMSE, when a  
472 particular variable is used for splitting nodes across all the trees in the RF.  
473 Specifically, RMSE is employed to assess the quality of splits, and to determine  
474 the importance of features in predicting output values.

### 475       **2.3.2. Data classification by clustering analysis**

476 The exploratory analysis of spatial large datasets is often performed by means of  
477 clustering techniques, aiming at identifying different classes in the data,  
478 accounting on the distribution of the variables under study. There are two types  
479 of clustering algorithms used for class identification purposes: algorithms based  
480 on the density of points and algorithms based on the distance between points. The  
481 algorithm used here is named k-means, and it is a distance-based procedure to  
482 cluster data, based on the number of desired clusters and their centroids. The  
483 algorithm assigns every element in the dataset to a cluster, iteratively minimizing  
484 the variance of the Euclidean distance of the elements of each cluster from their  
485 centroids. Consequently, the data labelling is done based on their geometrical

486 disposition in the dot cloud, depending on the target number of clusters to be  
487 identified (Lloyd, 1982; Arthur and Vassilvitskii, 2007). When variables with  
488 very different magnitudes are being related for clustering purposes, it is  
489 convenient to normalize the data keeping the relative distances between  
490 observations. Therefore, the clustering here is applied to the standardized data to  
491 exploit the variance of each variable and keeping the geometrical disposition  
492 between observations stable.

493 As the k-means algorithm does not automatically estimate the optimal number of  
494 clusters to be identified within the dataset, the Silhouette metric has been used  
495 here to evaluate the preferred number of clusters (Rousseeuw, 1987; de Amorim  
496 and Hennig, 2015). In fact, this metric quantifies the quality of cluster  
497 identification by scoring the difference between the overall average intra-cluster  
498 distances and the average inter-cluster distances related to the maximum between  
499 the latter two. In that way the metric would always be a value ranging from -1  
500 and 1, where typically 1 means that clearly distinguished clusters have been  
501 identified, 0 means that the identified clusters are indifferent, and -1 means that  
502 data are mixed in the identified clusters.

503 **3. Results and discussion**

504 The analysis is carried out on both field monitored and synthetic datasets, to  
505 quantify the information provided by the defined antecedent variables useful to  
506 predict the seasonal changes of the slope response to precipitation. The analysis  
507 of the physical behavior of the studied slopes is based on the results of model  
508 simulations, as if they satisfactorily resemble what could be measured in the field.  
509 Indeed, the uncertainty of model parameters may affect the identified cause-  
510 effect relationships. However, during the calibration of model, field  
511 measurements of the hydraulic behavior of the involved soil were considered  
512 (Greco et al., 2013), thus the major features of the hydrological processes  
513 occurring in the slope are considered reliably reproduced in the synthetic dataset.

514        **3.1. Role of measurable variables on the response of the soil mantle**

515        To select the most informative triplets of variables, for predicting the change in  
 516        water storage ( $\Delta S$ ) in the soil mantle, associated to rainfall events of total depth  
 517        H, four Random Forest models are trained to predict the ratio  $\Delta S/H$ , based on the  
 518        dataset consisting of all possible combinations of the synthetic variables:  
 519         $\langle H, \theta_6, h_a \rangle$ ,  $\langle H, \theta_{100}, h_a \rangle$ ,  $\langle H, \theta_6, \theta_{100} \rangle$  and  $\langle \theta_6, \theta_{100}, h_a \rangle$ . In fact, the change in  
 520        storage  $\Delta S$  is obviously strongly dependent on the event rainfall depth H (i.e., the  
 521        more it rains the more soil storage increases), thus concealing important  
 522        hydrological processes going on the slope. Differently, the choice of the ratio  
 523         $\Delta S/H$ , a measure of the amount of rain that remains stored in the soil mantle,  
 524        allows detaching the water drainage processes from the water accumulation  
 525        processes. For each Random Forest model, the values of the Root Mean Square  
 526        Error (RMSE) are calculated, and the importance of each predictor variable is  
 527        evaluated according to the procedure described in Section 2.3.1. The  
 528        computational effort implied in doing the calculations by a conventional  
 529        workstation with a Core(TM) i7-10870H processor and 16 GB of SDRAM  
 530        memory is less than 2 minutes for each model run. The obtained results are  
 531        reported in Table 2.

532        **Table 2. RMSE and variable importance for  $H$ ,  $\theta_6$ ,  $\theta_{100}$  and  $h_a$  in the prediction of**  
 533        **soil response described as  $\Delta S/H$**

Dataset	RMSE	Importance			
		H	$\theta_6$	$\theta_{100}$	$h_a$
$\langle H, \theta_6, h_a \rangle$	0.122	0.156	0.140	-	0.704
$\langle H, \theta_{100}, h_a \rangle$	0.120	0.143	-	0.164	0.693
$\langle H, \theta_6, \theta_{100} \rangle$	0.140	0.287	0.440	0.273	-
$\langle \theta_6, \theta_{100}, h_a \rangle$	0.124	-	0.101	0.133	0.766

535 All the choices of triplets indicate that all the tested variables are informative to  
536 predict the normalized soil mantle response  $\Delta S/H$  (Table 2), with the perched  
537 ground water level,  $h_a$ , resulting the most influent variable. The importance of  
538  $h_a$  on the response of the soil mantle suggests that, in some conditions, the change  
539 in soil storage is affected by the effectiveness of water exchange between the soil  
540 mantle and the underlying aquifer, as it will be discussed in the following  
541 sections. Moreover, in Table 2 the triplet showing the lowest RMSE values is  
542 formed by the total rainfall depth, the aquifer water level, and the mean  
543 volumetric water content in the uppermost 100 cm. According to the Random  
544 Forest model, they are the most informative for predicting the soil mantle  
545 response. Therefore, the triplet  $\langle H, \theta_{100}, h_a \rangle$  is used for further analysis.

546 Considering the triplet of input variables  $\langle H, \theta_{100}, h_a \rangle$ , a variance-based  
547 Sensitivity Analysis has been also carried out, based on the methodology outlined  
548 by Sobol (2001), which is implemented in the Sensitivity Analysis Library in  
549 Python - SALib toolbox (Herman and Usher, 2017; Iwanaga et al., 2022). The  
550 sampling scheme proposed by Saltelli (2002) has been used to generate 65536  
551 triplets, so to have a similar number of data as for the RF importance analysis.  
552 Table 3 reports the obtained sensitivity indices.

553 **Table 3. Sensitivity indices of the variance-based SA of the variability of  $\Delta S/H$**   
554 **resulting from variations of  $H$ ,  $\theta_{100}$  and  $h_a$**

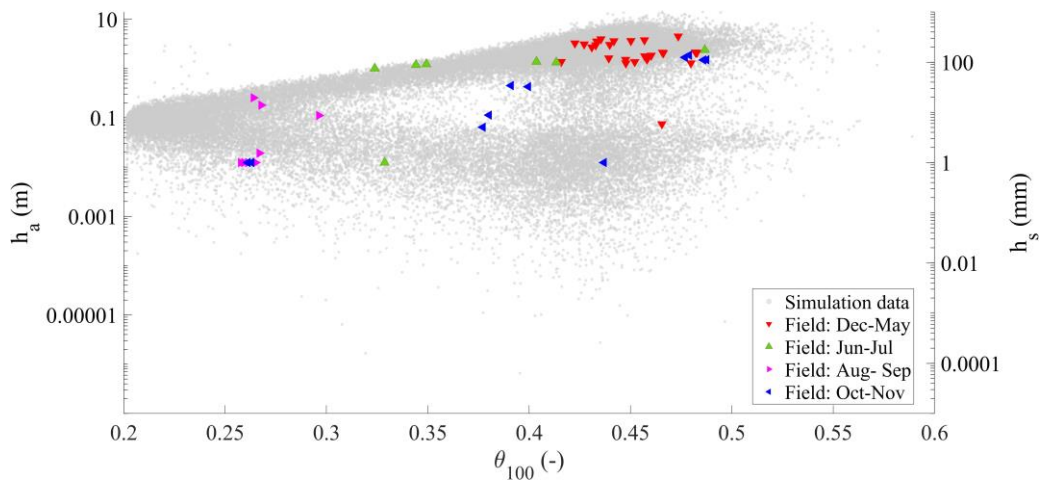
Variable	$S_{tot}$	$S_1$ (single parameter variations)	$S_2$ (mutual interactions)	
$\theta_{100}$	0.532	0.471	$(\theta_{100}, h_a)$	0.002
$h_a$	0.058	0.058	$(\theta_{100}, H)$	0.060
$H$	0.469	0.412	$(h_a, H)$	0.000

555

556 Interestingly, the indices show how the aquifer water level,  $h_a$ , which is the most  
557 informative variable for output predictions according to the RF analysis, is  
558 responsible only for a small part of the output variability, which instead is mostly  
559 related to the variations of the other two input variables. As it will be discussed  
560 in sections 3.2 and 3.3,  $h_a$ , not affecting the variability of  $\Delta S/H$ , is anyway an  
561 extremely informative variable, as it allows separating the initial conditions in  
562 two families: low levels and high levels, corresponding to quite different  
563 responses of the soil mantle to precipitation. It also arises that output variability  
564 mostly depends on the variations of single inputs (i.e., the indices  $S_1$  explain most  
565 of the total sensitivity, and the indices  $S_2$ , measuring the contribution to the total  
566 output variance deriving from mutual interactions between couples of inputs are  
567 all small).

568       **3.2. Soil and underground antecedent conditions**

569 The field monitoring activities allow to get a complete dataset that traces the  
570 rainfall values coupled with the soil mean volumetric water content in the  
571 uppermost meter of the soil profile ( $\theta_{100}$ ) and the water depth of the Castello  
572 stream ( $h_s$ ), both measured hourly for three years. The field monitored data,  
573 composed by 57 rainfall events, include the water level of the Castello stream  
574 rather than the direct measurement of the aquifer water level ( $h_a$ ). Nevertheless,  
575 a direct relationship links the water level in the aquifer and the water level in the  
576 stream, as assumed for the mathematical modelling. This dataset has been  
577 enriched synthetically, as it has been described in section 2.2.



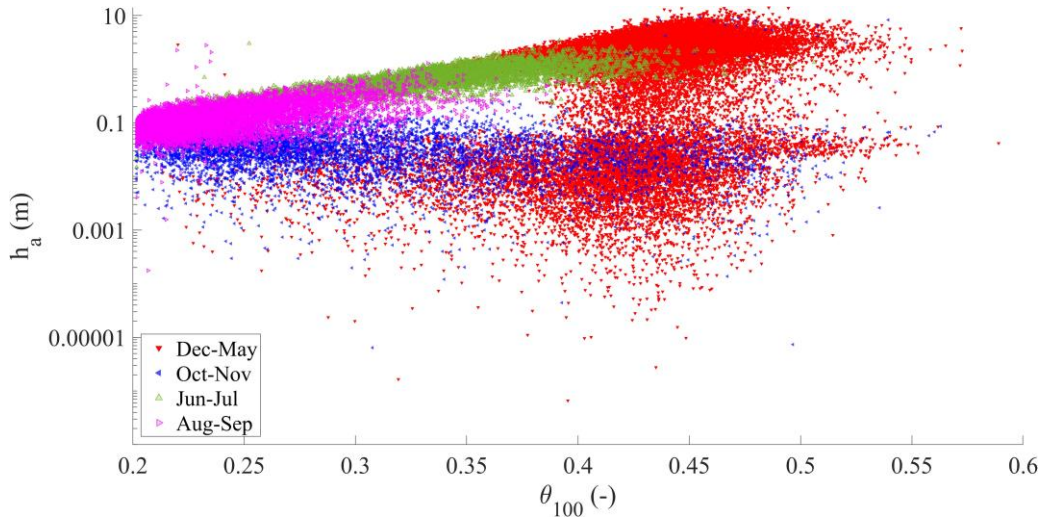
580     **Figure 5. Field monitored mean volumetric water content in the upper meter of the**  
 581     **soil profile ( $\theta_{100}$ ) and water depth in the Castello stream ( $h_s$ ), compared with**  
 582     **synthetic data of  $\theta_{100}$  and aquifer water level ( $h_a$ ) (on the vertical axis, plotted in**  
 583     **logarithmic scale to help visualizing of small water levels and thus not allowing to**  
 584     **represent zeroes, the values of  $h_s$  smaller than the sensitivity of the water level**  
 585     **sensor have been plotted as 1 mm; also the smallest simulated values of  $h_a$  should**  
 586     **be considered equivalent to zero, owing to the limits of any measurement device,**  
 587     **which could be used for operational field monitoring).**

588     Therefore, to analyze the effects of the underground conditions on the slope  
 589     response, Figure 5 shows the simulated data (circular dots in the background) and  
 590     the field monitored data (triangular colored dots). Logarithmic axes are used to  
 591     distinguish the very low aquifer water level from the high values.

592     Four major seasonally recurrent conditions could be identified for the water in  
 593     the subsurface system from field monitored data: first, a condition usually  
 594     occurring between December and May is characterized by the highest water  
 595     content in the soil and the highest measured water level in the stream. Second,  
 596     the period from June to July is characterized by intermediate water content  
 597     values, with still high level in the stream. Third, the period from August to  
 598     September is characterized by the lowest values of water content in the soil, but  
 599     also the lowest water depth  $h_s$  measured in the stream (few centimeters, in some

600 cases nearly zero). Finally, the period from October to November is characterized  
601 by a wide range of values in soil water content and a relatively low range of  
602 stream water depth.

603



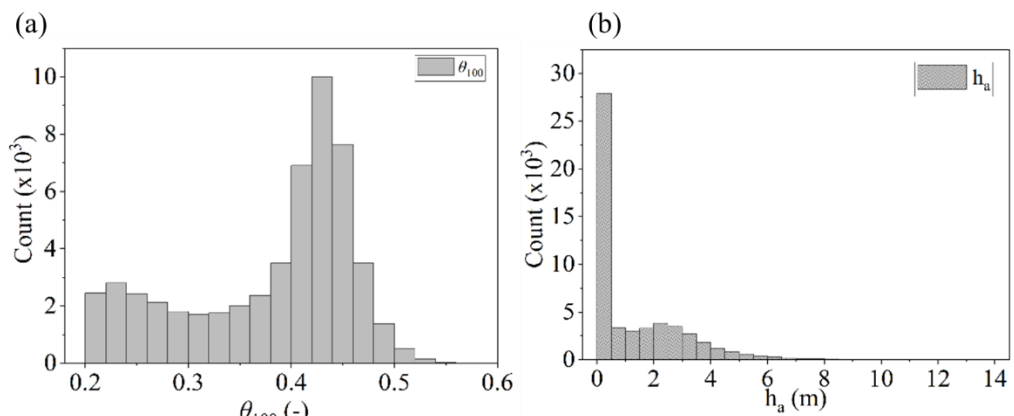
604

605 **Figure 6. Seasonal behavior of the aquifer water level ( $h_a$ ) and the mean volumetric**  
606 **water content of the upper meter of the soil profile ( $\theta_{100}$ ) for the synthetic dataset**  
607 **(the vertical axis is plotted in logarithmic scale to help visualizing small water**  
608 **levels).**

609 The underground antecedent conditions are naturally linked to a seasonal  
610 behavior dominated by the hydrological conditions which can be traced in time  
611 as it can be seen from the synthetic data (Figure 6). The months from December  
612 to April follow a winter and spring behavior, characterized by wet soil conditions  
613 and aquifer water levels ranging from low to high. From June to July, a late spring  
614 behavior is visible, characterized by relatively dry soil (i.e., most of the data  
615 falling below soil field capacity), in combination with relatively high  
616 groundwater levels (indicating a still active slope drainage). In August and  
617 September, a summer like behavior is shown, with the driest soil water content  
618 and generally low aquifer water level. Finally, in October and November, the end

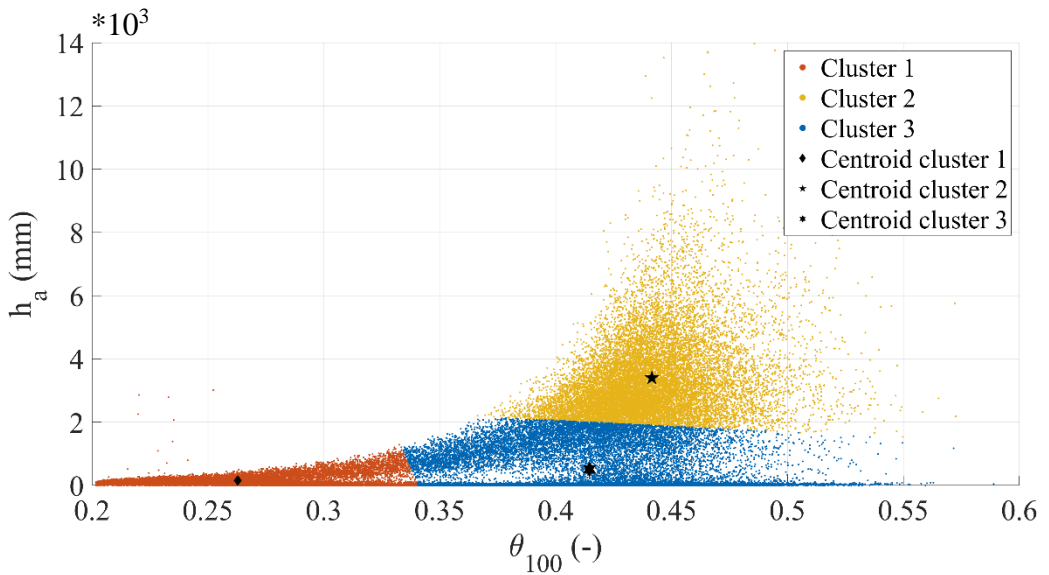
619 of the dry season is shown: a wide range of soil wetness coupled with a still low  
620 aquifer water level.

621 For both the field monitored and synthetically obtained datasets, the observed  
622 conditions are the result of the time lag between the beginning of the rainy season  
623 and the slope response. The recurrent seasonal behavior observed for the  
624 synthetic dataset, although delayed or anticipated owing to the year-by-year  
625 variability of rainfall, is close to that observed in the field.



626  
627 **Figure 7. Histograms for data distributions of (a)  $\theta_{100}$  and (b)  $h_a$  for the synthetic**  
628 **dataset**

629 The overall situation for the synthetic dataset of antecedent conditions (i.e.,  
630 duplets  $\langle \theta_{100}, h_a \rangle$ ) can be described by the distribution of each individual  
631 variable, which can be seen in the histograms shown in Figure 7. It is interesting  
632 to note that, for both  $\theta$  and  $h_a$ , a bimodal behaviour is observed, corresponding  
633 to dry and wet field conditions.

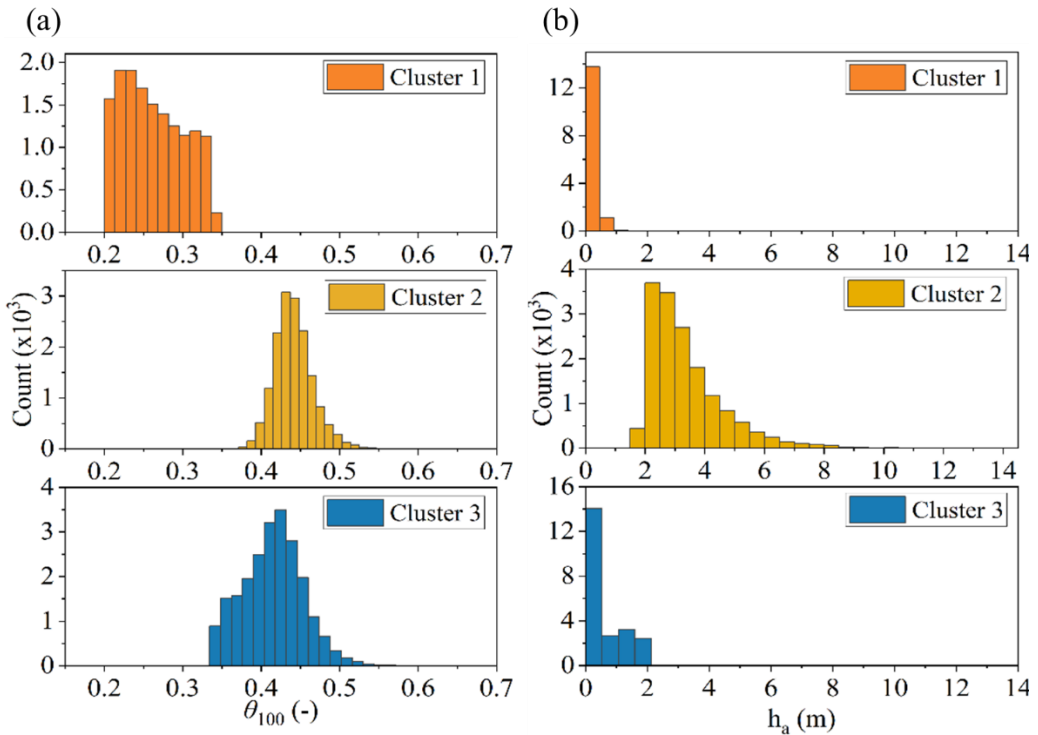


634

635   **Figure 8. Identified clusters for the duplets  $\langle \theta_{100}, h_a \rangle$  representing underground**  
 636   **antecedent conditions of the synthetic dataset. For each cluster, the centroids are**  
 637   **shown.**

638   The k-means clustering technique has been used to investigate the geometrical  
 639   distribution of the duplets  $\langle \theta_{100}, h_a \rangle$ , with number of clusters ranging from 2 to  
 640   7. According to the Silhouette metric, the optimal number of clusters is 3, with a  
 641   metric value of 0.7, allocating the 28%, 30% and 42% of the data in clusters 1, 2  
 642   and 3 respectively. Figure 8 shows the 3 clusters obtained within the synthetic  
 643   dataset. Centroid positions are also displayed, showing the zones of the clouds  
 644   where most of the dots are gathered. This representation of the data use both  
 645   vertical and horizontal axes in linear scale to let visualize distance magnitudes  
 646   between the different clusters, but it corresponds to the same dataset shown in  
 647   Figure 6.

648   The distribution of the data after clustering is also analyzed for each cluster and  
 649   the histograms are shown in Figure 9. It looks clear that the clusters capture  
 650   different couplings of dry and wet underground antecedent conditions.



651

652 **Figure 9. Histograms for data distributions of (a)  $\theta_{100}$  and (b)  $h_a$ , according to each**  
 653 **identified cluster in the duplets  $(\theta_{100}, h_a)$**

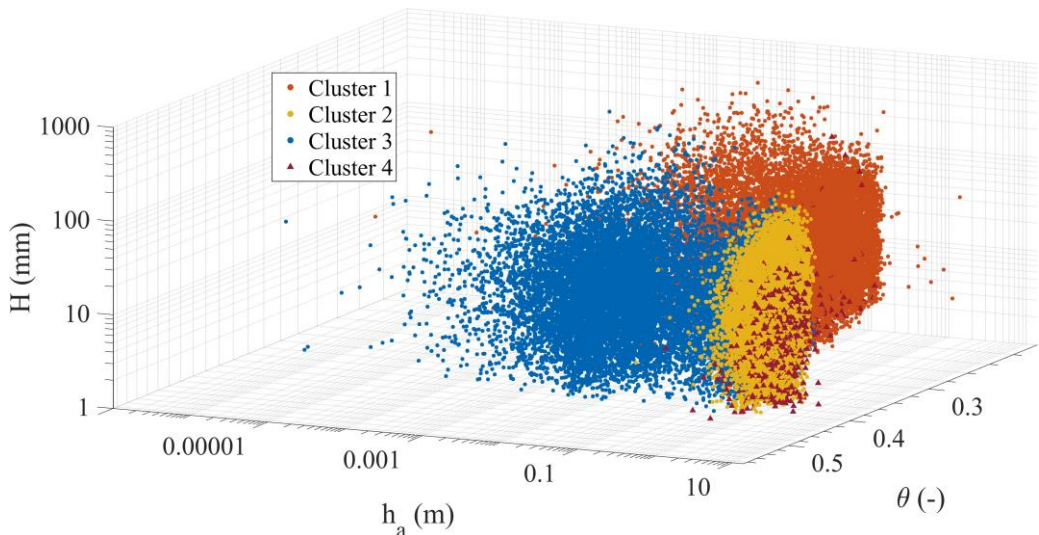
654 In fact, cluster 1 captures dry conditions, with a volumetric water content below  
 655 the field capacity  $\theta_{fc}$  (it was estimated as 0.35 with the empirical relationship  
 656 proposed by Twarakavi et al. (2009) according to the van Genuchten model  
 657 parameters) and low values of  $h_a$ . Differently, clusters 2 and 3 capture scenarios  
 658 related to relatively wet soil mantle conditions (i.e.,  $\theta_{100} > \theta_{fc}$ ), coupled to low  
 659  $h_a$  in cluster 3, gathering scenarios normally observed in late autumn, and to the  
 660 highest  $h_a$  conditions for cluster 2, comprising conditions normally occurring in  
 661 late winter and spring.

662 The two chosen variables,  $\theta_{100}$  and  $h_a$ , allow identifying three different  
 663 antecedent slope conditions one hour before the onset of any rainfall event.  
 664 Hence, it is worthy to investigate how these different antecedent conditions may  
 665 be related to different slope responses to precipitation.

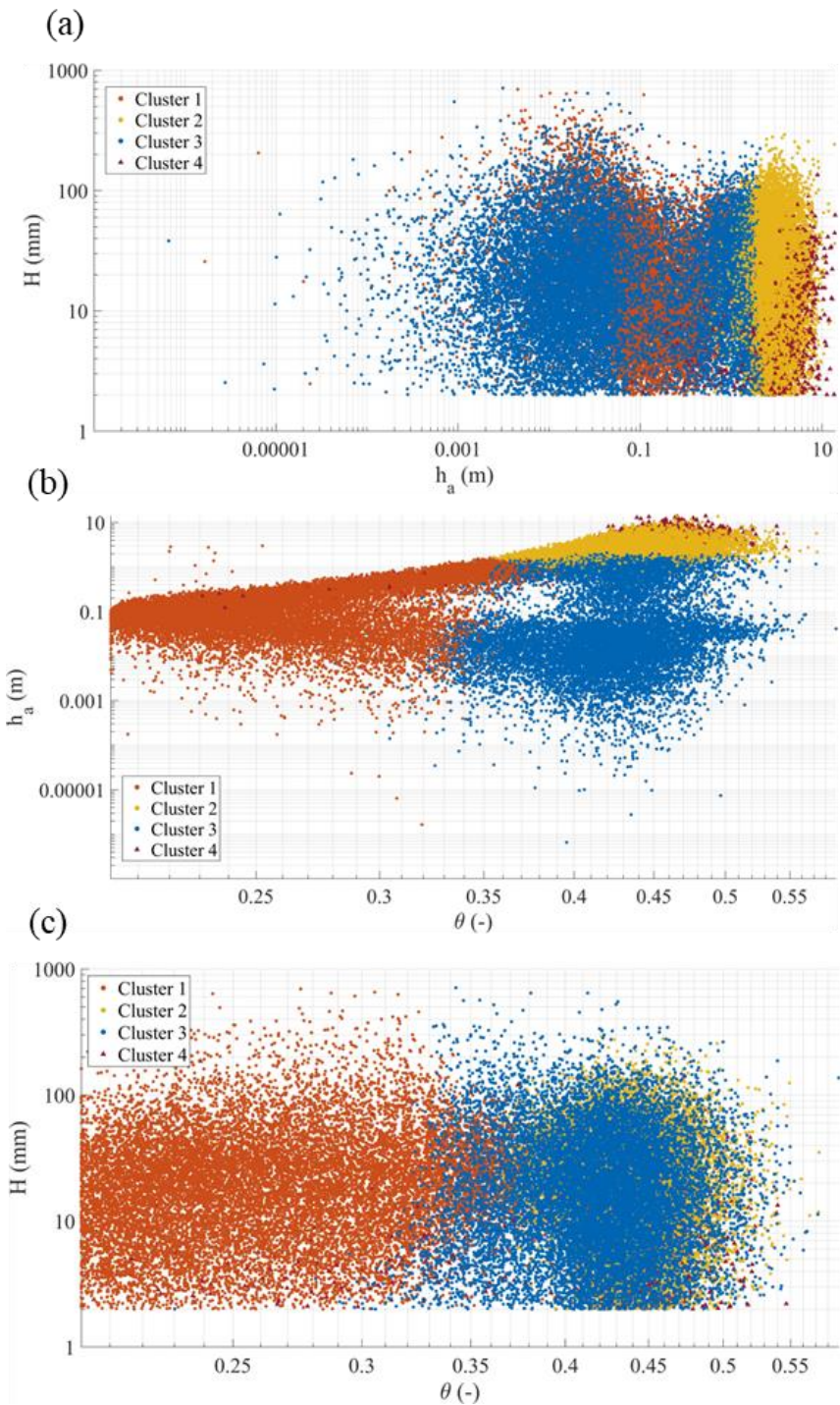
666       **3.3. Effects of soil and underground antecedent conditions on the**  
667       **slope response to rainfall**

668       The analysis of the data has been focused on identifying clusters within the  
669       triplets  $\langle \theta_{100}, h_a, \Delta S/H \rangle$ , aiming to evaluate the slope response as the amount of  
670       rainwater being stored/drained in the soil mantle. The results are being plotted in  
671       the space composed by the variables that can be monitored in the field:  
672        $(\theta_{100}, h_a, H)$ .

673       As it is not always expected to experience increased soil storage during rainfall  
674       events, the identification of draining slope conditions is an important aspect.



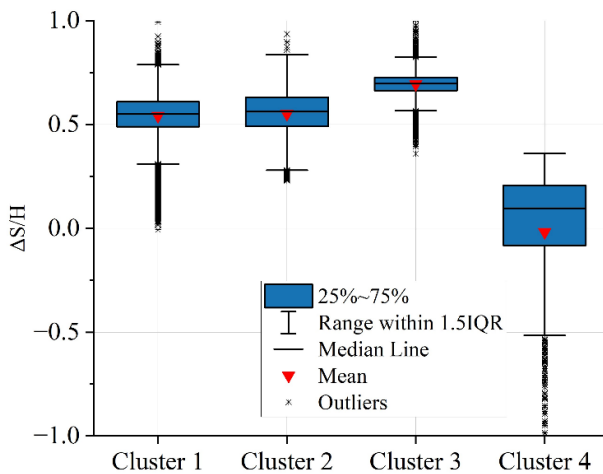
676       **Figure 10. Clustering results of the synthetic data triplets  $\langle \theta_{100}, h_a, \Delta S/H \rangle$**   
677       **represented in the space  $(\theta_{100}, h_a, H)$**



679

680      **Figure 11. Clustering results of the triplets  $\langle \theta_{100}, h_a, \Delta S/H \rangle$  in (a)  $(\theta_{100}, h_a)$  plane;**  
 681      **(b)  $(\theta_{100}, H)$  plane; (c)  $(H, h_a)$  plane**

682 Figure 10 and Figure 11 show the data clusters for the triplets  $\langle \theta_{100}, h_a, \Delta S/H \rangle$ ,  
 683 for any identified rainfall event, represented in the  $(\theta_{100}, h_a, H)$  space in a  
 684 logarithmic axis representation. The Silhouette metric in this case suggests 4 as  
 685 an optimal number of clusters with a metric value of 0.61. It is remarkable that  
 686 three of the clusters are close to those already identified from the antecedent  
 687 (seasonally recurrent) underground conditions (section 3.2).



688 **Figure 12. Distribution of the slope response  $\Delta S/H$  for the data in each cluster**

689 Specifically, cluster 1, 2 and 3 correspond to different slope processes according  
 690 to  $\Delta S/H$  (Figure 12). Even if cluster 1 and cluster 2 show similar responses, with  
 691 slightly smaller  $\Delta S/H$  for cluster 1, the controlling processes are indeed different;  
 692 the conditions of cluster 1 are typically occurring in dry seasons with long dry  
 693 periods between short rainfall events, leading to dry antecedent conditions, so  
 694 that accumulation of water in the soil mantle (increase in water storage) is  
 695 expected at each event. The data in cluster 2 are typically related to wet seasons,  
 696 especially in late winter and spring, where rainfall events are more frequent,  
 697 leading to antecedent wet soil ( $\theta_{100} \geq \theta_{fc}$ ) and antecedent high ground water  
 698 level. However, these conditions do not seem to correspond to effective slope  
 699 drainage, so that the slope response in cluster 2 results comparable to that  
 700 observed in cluster 1 in terms of  $\Delta S/H$ . Instead, the conditions gathered in cluster

702 3 differ from those in cluster 2 for the lower aquifer water level  $h_a$ , and the  
703 highest  $\Delta S/H$  indicates the lowest slope drainage.

704 The additional cluster 4 identified here highlights a particular slope response, as  
705 it catches all the conditions where nearly zero and negative  $\Delta S$  take place,  
706 meaning an effective slope drainage during rainfall events. It is interesting to note  
707 that, even for relatively high rainfall events (above 100 mm), this slope response  
708 occurs when soil moisture is above the field capacity and when this condition is  
709 coupled with very high groundwater level, probably due to the high permeability  
710 all along the soil mantle and to the hydraulic connection with the underlying  
711 aquifer.

#### 712 4. Conclusions

713 This study aims at identifying and analysing the major hydrological controls of  
714 the slope response to precipitation and, in that way, defining suitable variables to  
715 be monitored in the field to predict such response. The studied case refers to the  
716 hydrological processes in a slope system consisting of a pyroclastic soil mantle  
717 overlaying a fractured karstic bedrock, where a perched aquifer develops during  
718 the rainy season. A synthetic time series of slope response to precipitation has  
719 been built, thanks to a physically based model, previously calibrated with field  
720 monitoring data, coupled with a stochastic rainfall generator. Synthetic and  
721 experimental data show substantial agreement. In fact, the soil water content  
722 values measured in the field are close to those of the synthetic dataset.  
723 Furthermore, the simulated epikarst water level shows similar seasonal behaviour  
724 as the stream level records, indeed directly related with the discharge from the  
725 epikarst aquifer. The synthetic dataset has been explored with Random Forest  
726 and k-means clustering, to evaluate the slope response characterized as the  
727 change in water stored in the soil mantle ( $\Delta S$ ) during precipitation events with  
728 rainfall depth  $H$ , starting from different underground antecedent conditions.  
729 These were quantified through the mean volumetric water content in the

730 uppermost meter of soil mantle ( $\theta_{100}$ ) and the aquifer water level ( $h_a$ ), one hour  
731 before the onset of rainfall.

732 The ratio  $\Delta S/H$ , which allows identifying soil mantle response regardless the  
733 amount of event precipitation, is sensitive to both  $h_a$  and  $\theta_{100}$ , with the  
734 groundwater level being the most influential antecedent variable. The  
735 underground antecedent conditions, characterized by  $\theta_{100}$  and  $h_a$  and linked to  
736 the seasonal meteorological forcing, allow identifying different responses,  
737 related to the seasonally active hydrological processes.

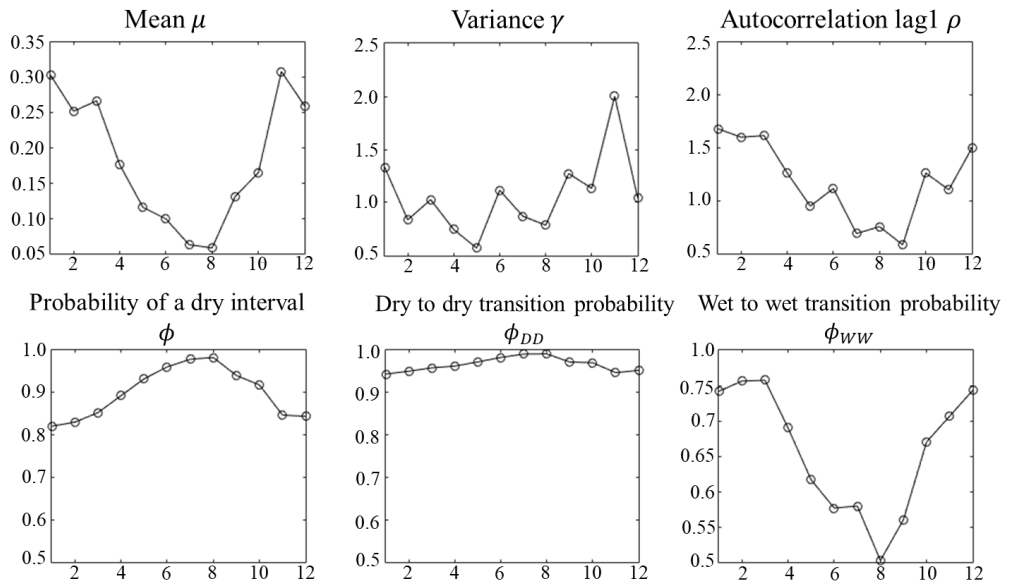
738 High perched groundwater level, typical of winter and spring, indicates active  
739 drainage from the soil mantle, which compensates rainwater infiltration, so that  
740 the soil storage remains stable, or even reduces, even after large rainfall events.

741 Differently, low perched groundwater level corresponds to impeded drainage.  
742 When it occurs with initially dry soil mantle (typically in summer and early  
743 autumn), it tends to retain all the infiltrated rainwater as increased soil storage.  
744 When the soil mantle is already wet (i.e., above the field capacity) at the onset of  
745 rainfall events, as it usually happens in late autumn and early winter, the increase  
746 of soil storage is smaller, as the soil approaches saturation.

747 The presented results suggest that monitoring antecedent conditions, by  
748 measuring suitable variables to identify the major hydrological processes  
749 occurring in the slope in response to precipitation, can be useful to understand  
750 such processes and to develop effective predictive models of slope response.  
751 Therefore, the proposed methodology can be replicated also in other contexts and  
752 be useful for several hydrologic applications: from the water supply towards  
753 natural streams due to infiltrated water, to the hydric stress estimation in crops  
754 (e.g., the centenary chestnut forests of the case study) especially in very dry  
755 seasons, but also for the design of effective monitoring networks exploiting  
756 geohydrological information for geohazard prevention (and early warning).

757 **Appendix A: Calibration of the Stochastic Rainfall Generator**

758 The Neyman-Scott Rectangular Pulse (NSRP) model (Neyman and Scott, 1958;  
759 Rodriguez-Iturbe et al., 1987; Cowpertwait et al., 1996) is here used as stochastic  
760 rainfall generator. The NSRP describes the process of point rainfall as a  
761 superposition of randomly arriving rain clusters, each containing several rain  
762 cells with constant intensity. The hyetograph within a cluster is obtained by  
763 summing the intensity of the various cells belonging to the cluster. It has been  
764 calibrated based on 17 years of experimental data (2000-2016) of rainfall depth  
765 at 10 min time resolution, recorded by the rain gauge managed by the Civil  
766 Protection in Cervinara (Southern Italy). The calibration has been carried out by  
767 minimizing, for rainfall aggregated at various durations, the difference between  
768 the following quantities, estimated by the model and calculated from the  
769 experimental data: mean, variance, lag 1 autocorrelation, probability of dry  
770 interval, probability of transition from dry-to-dry interval and probability of  
771 transition from wet-to-wet interval. The calibration procedure, based on the one  
772 proposed by Coptwertwait et al. (1996), is described in detail in Peres and  
773 Cancelliere (2014). To account for the seasonality of rainfall, these quantities  
774 have been calculated month by month in the experimental record (Figure A1),  
775 suggesting that the calibration of the NRSP model should be carried out  
776 separately for seven homogeneous periods (September, October, November,  
777 December-March, April, May-June, July-August).



778

779 **Figure A1. Monthly plot of hourly rainfall characteristics calculated based on the**  
 780 **experimental data of the rain gauge of Cervinara.**

781 Table A1 gives the obtained parameters of the NSRP stochastic model, where  $\lambda$   
 782 represents the parameter of a Poisson process describing the arrival of clusters;  $v$   
 783 is the mean number of cells in a cluster, also described by a Poisson process;  $\beta$  is  
 784 the parameter of an exponential probability distribution describing the arrival  
 785 times of each cell in a cluster, expressed as the number of time intervals of 10  
 786 minutes starting from the beginning of a cluster;  $\eta$  is the parameter of an  
 787 exponential probability distribution describing the duration of rain cells;  $\xi$  is the  
 788 parameter of a Weibull probability distribution describing the rain intensity of  
 789 cells, with cumulative probability function  $F(x, \xi, b) = 1 - \exp(-\xi x^b)$ , in which  
 790  $x$  is cell rain intensity and the parameter  $b = 0.8$  has been set a priori  
 791 (Cowpertwait et al., 1996).

792

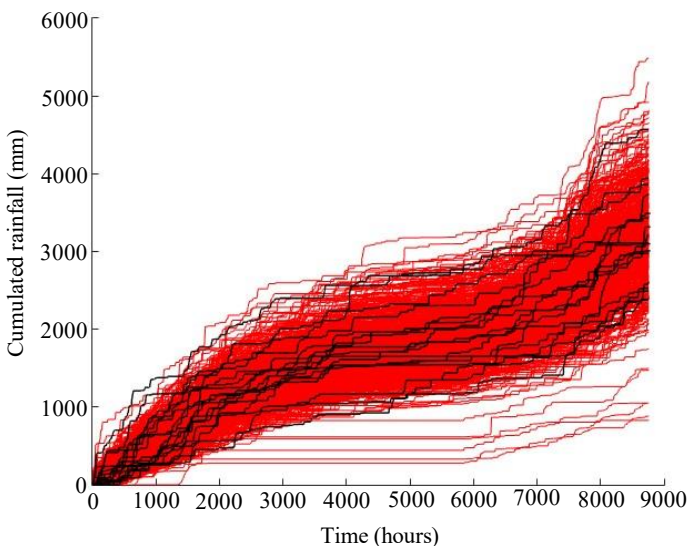
793

794

795 **Table A1. Parameters of the NSRP model.**

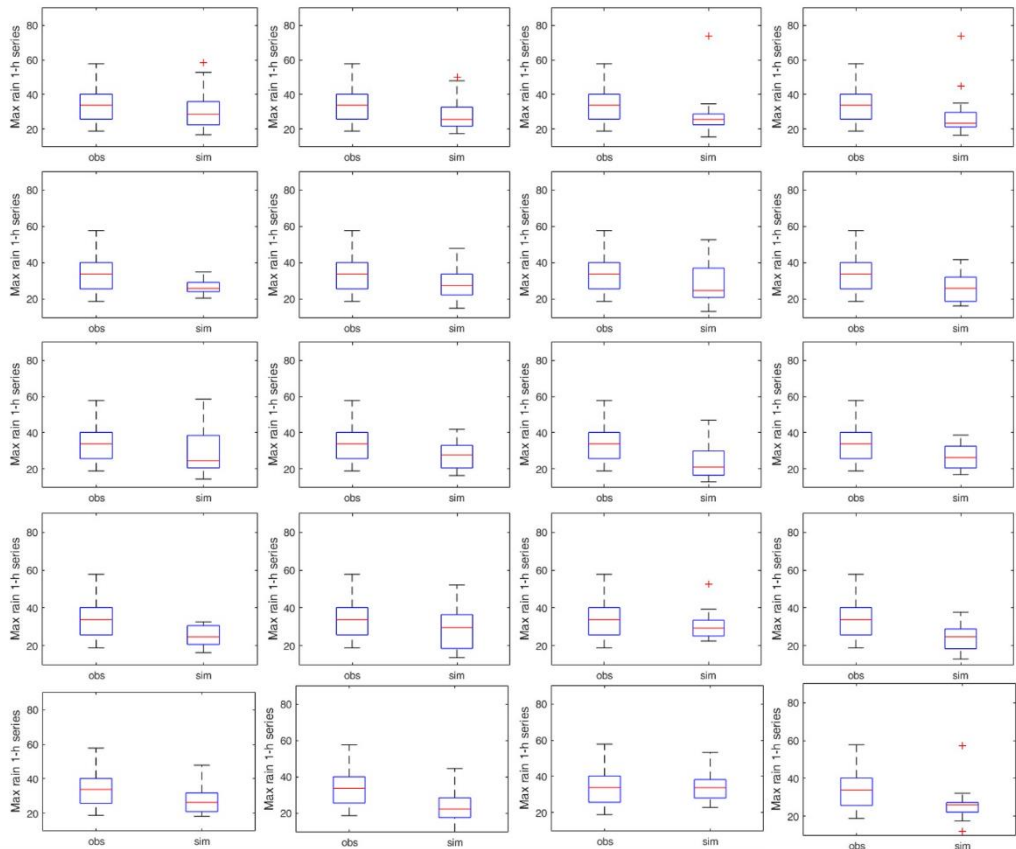
Param .	Sept	Oct	Nov	Dec-Mar	Apr	May-Jun	Lug.Aug
$\lambda$ ( $\text{h}^{-1}$ )	0.01 5	0.0052 4	0.0025 7	0.0238	0.0080 9	0.00386	0.00900
$v$ (-)	2.68	36.4	57.1	2.60	38.7	21.6	1.40
$\beta$ ( $\text{h}^{-1}$ )	0.26 5	0.156	0.0167	0.813	0.123	0.116	24.5
$\eta$ ( $\text{h}^{-1}$ )	1.41	57.3	1.43	0.280	15.5	8.59	1.23
$\xi$ ( $\text{h}^b$ $\text{mm}^{-b}$ )	0.33 0	0.047	0.450	0.967	0.186	0.158	0.268

796 The adherence of the rainfall generated with the stochastic model to the  
 797 experimental rainfall data has been tested by evaluating rainfall characteristics  
 798 different from those used for the calibration. For instance, Figure A2 shows the  
 799 comparison of the rainfall depth, cumulated over one year, for the experimental  
 800 data (17 years) and for 1000 years of synthetic data generated with the calibrated  
 801 NSRP model.



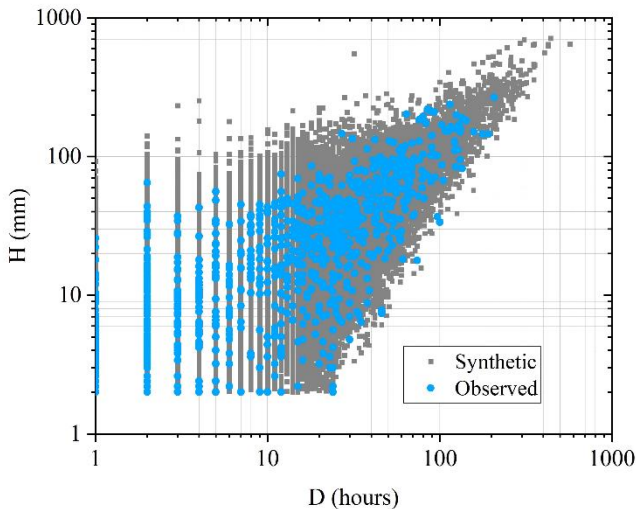
802  
 803 **Figure A2. Comparison of observed (black) and simulated (red) cumulated rainfall**  
 804 **plots in a year.**

805 In Figure A3, the boxplot of the maximum hourly rainfall in one year, observed  
 806 in the experimental dataset of 17 years, is compared with the same boxplot  
 807 referred to 20 series of 17 years randomly extracted from the generated 1000  
 808 years synthetic rainfall series. Several of the synthetic 17 years intervals show a  
 809 distribution of the maximum hourly rainfall close to the observed one.



810

811 **Figure A3. Comparison of observed and simulated distributions (boxplots) of the**  
 812 **maximum hourly precipitation in a year, for series of the same length. Each panel**  
 813 **shows the distribution for the 17 observed years (boxplot is always the same), and**  
 814 **17 randomly picked simulated years.**

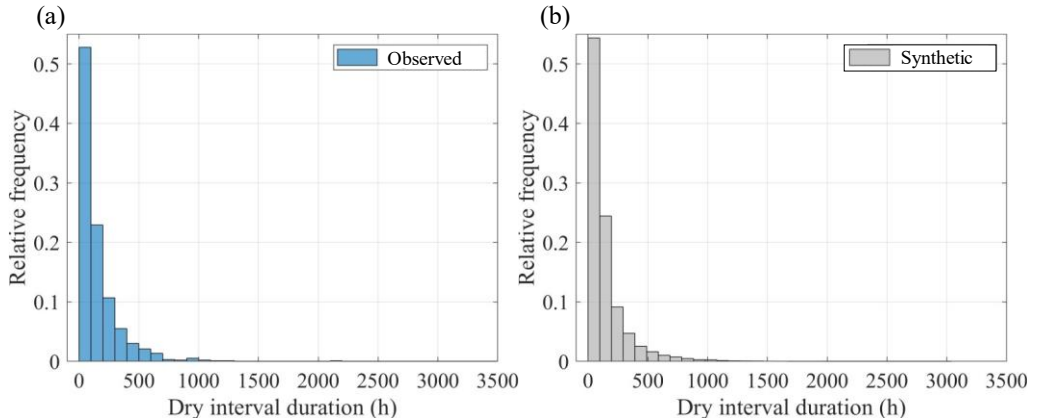


815

816 **Figure A4.** Scatterplot of total rainfall event depth (H) vs. rainfall event duration  
 817 (D). The events have been sorted within the rainfall datasets by considering a  
 818 separation “dry” interval of 24 hours with less than 2 mm rainfall. The blue dots  
 819 represent events extracted from the 17 years experimental rainfall dataset, while  
 820 the grey dots represent events extracted from the 1000 years synthetic rainfall  
 821 dataset.

822 Regarding the required comparison between synthetic and observed wet and dry  
 823 intervals, figure A4 shows the scatterplot of duration and total rain depth of the  
 824 events, sorted with a separation “dry” interval of 24 hours with less than 2 mm  
 825 rainfall from the observed dataset (blue dots) and the synthetic dataset (grey  
 826 dots). The plots show how the synthetic data contain the observed ones, and that  
 827 the shape of the dot clouds looks quite similar.

828 Figure A5 shows the frequency distributions of the durations of dry intervals  
 829 belonging to the 17 years rainfall dataset, and the same distribution for the dry  
 830 intervals extracted from the 1000 years synthetic dataset: the two distributions  
 831 look nearly identical.



832

833 **Figure A5. Frequency distributions of dry interval durations for events extracted**  
 834 **from the 17 years experimental rainfall dataset (a) and events extracted from the**  
 835 **1000 years synthetic rainfall dataset (b). The events have been sorted within the**  
 836 **rainfall datasets by considering a separation “dry” interval of 24 hours with less**  
 837 **than 2 mm rainfall.**

838

839 **Appendix B: Tuning Random Forest hyperparameters**

840 The Random Forest (RF) algorithm (Breiman, 2001) has been very successful as  
841 a general-purpose classification and regression method. Starting from Bagging  
842 or Bootstrap Aggregation (Efron and Tibshirani, 1993), RF builds several random  
843 de-correlated decision trees and then averages their predictions.

844 The regression RF algorithm can be summarized as follows: 1) by means of  
845 bootstrap, a sample is extracted from the training data; 2) based on the  
846 bootstrapped data, a tree  $T$  of the random-forest is grown by repeating the  
847 following operations until a leaf node (a node without split) is reached: a) for  
848 each node,  $m$  variables are randomly selected from the  $p$  input variables or  
849 features (with  $1 \leq m \leq p$ ); b) among the  $m$  variables, the best variable and  
850 splitting point are selected according to a minimum criterium; c) the node is split  
851 into two daughter nodes. To build the RF with  $B$  trees, steps 1 and 2 are repeated  
852  $B$  times. Then, the prediction,  $Y_{pred}$ , for a new observation,  $X$ , is the average of  
853 the final values,  $T_b(X)$ , i.e., the values of the predicted variable corresponding to  
854 the leaves of each tree:

855 
$$Y_{pred} = \frac{1}{B} \sum_{b=1}^B T_b(X) \quad (\text{B.1})$$

856 The main advantage of RF is the simplicity with which a forest can be trained,  
857 and the parameters of the algorithms optimized. In this paper, the scikit-learn  
858 framework (Pedregosa et al, 2011) is used to run the RF algorithm.

859 The main hyperparameters of a RF are: 1) n\_estimators: the number of trees of  
860 the forest; 2) max\_depth: the maximum depth of each decision tree in the forest;  
861 3) min\_samples\_leaf: the minimum number of samples required to be at a leaf  
862 node; max\_features: the number of features, or input variables, to consider when  
863 looking for the best split.

864 The procedure applied in this study to estimate and optimize the hyperparameters  
865 of the RF algorithm consists of the following steps:

866 - Step 1: the dataset is divided into a training set and a test set, respectively  
867 containing 80% and 20% of the data, randomly chosen.

868 - Step 2: the K-fold cross-validation technique (Stone, 1974), with K=10,  
869 is applied to empirically determine a set of values for the  
870 hyperparameters, using only the training dataset.

871 - Step 3: for each fold, a RF is trained on the other k-1 folds of the data and  
872 tested on the first fold. This process is repeated k=10 times, so to use each of  
873 the k folds exactly once as the validation set. A performance metric is then  
874 calculated for each fold, to estimate how well the RF will perform on new  
875 data. In this work the Root Mean Square Error (RMSE) is used as the  
876 performance metric.

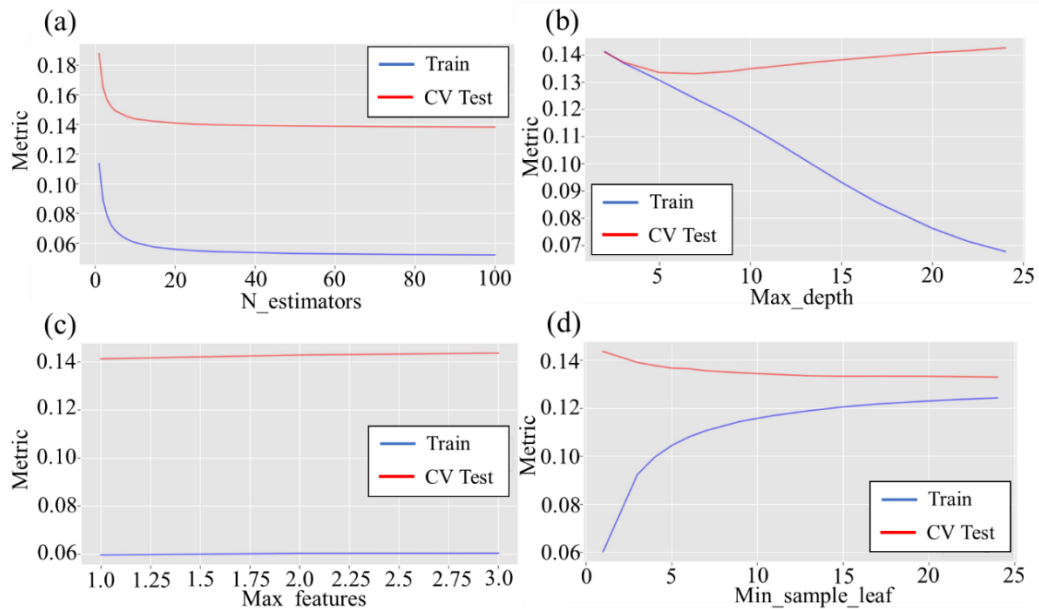
877 - Step 4: the RF is trained by changing one hyperparameters at once and using  
878 the default values for the other three (default values of hyperparameters as  
879 reported in Pedegrosa et al (2011) are: n\_estimators=100; max\_depth=*none*,  
880 i.e., the tree is expanded until all leaves contain less samples than  
881 min\_samples\_split; min\_samples\_leaf=1; max\_features=1).

882 - Step 5: from the results of the previous step, the ranges of hyperparameters,  
883 given in table B1, are defined. These values represent the grid in which the  
884 optimal hyperparameters are searched. In other words, using the K-fold  
885 technique (step 2), RF model is fitted K times, and then the optimal set of  
886 values is the one minimizing the RMSE.

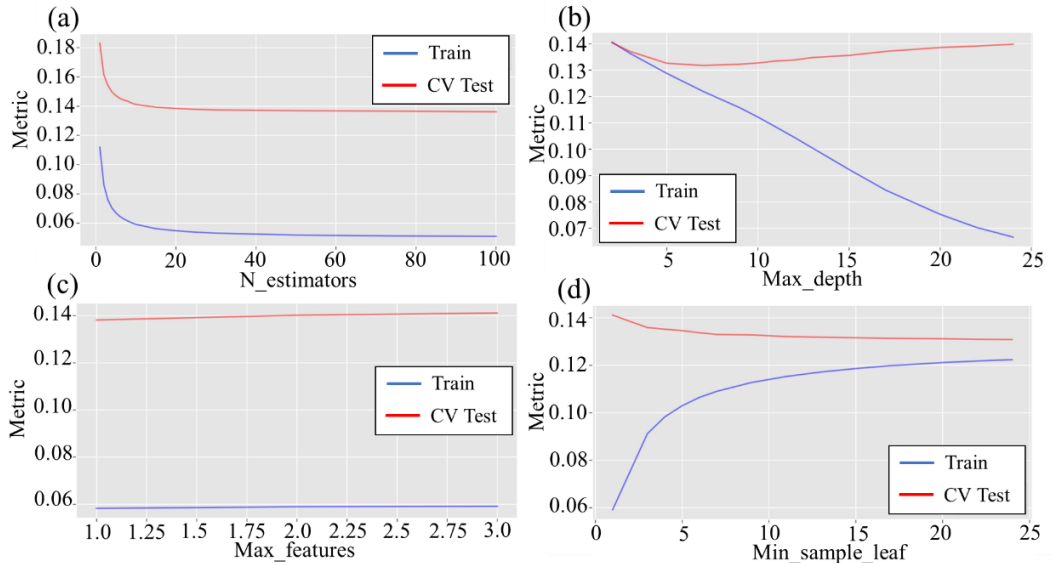
887 - Step 6 (validation of the model), once the optimal values of the  
888 hyperparameters are determined, the performance of RF model is evaluated,  
889 for the test dataset as defined in Step 1, using the RMSE.

890 In this study, the described methodology is used to evaluate the hyperparameters  
891 for the following RF models: RF1, trained using the input features  $\langle H, \theta_6, h_a \rangle$ ;

892 RF2, trained using  $\langle H, \theta_{100}, h_a \rangle$ ; RF3, trained using  $\langle H, \theta_6, \theta_{100} \rangle$ ; RF4, trained  
 893 using  $\langle H, \theta_6, \theta_{100} \rangle$ . All models are trained to predict the normalized change of  
 894 water storage in the soil mantle,  $\Delta S/H$ . Figures B1, B2, B3 and B4 show the  
 895 results of step 4. Specifically, they depict the trends of the RMSE versus the  
 896 hyperparameters for RF1, RF2, RF3 and RF4, respectively.

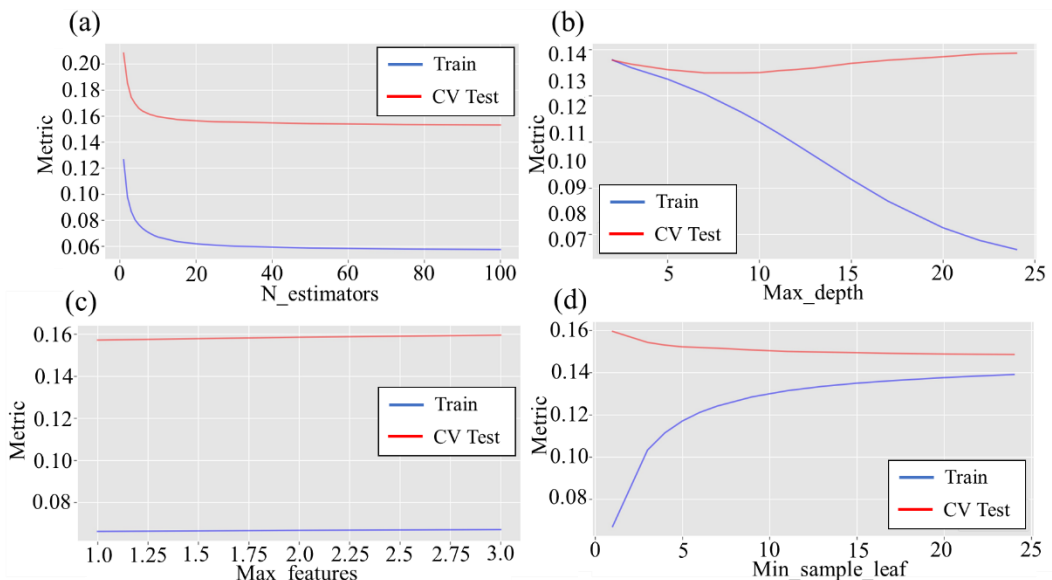


897  
 898 **Figure B1. Performance of random forest model RF1 on the test and Cross**  
 899 **Validation (CV) sets according to the test metric by changing the hyperparameters:**  
 900 **(a) N\_estimators (b) Max\_depth (c) Max\_features (d) Min\_samples\_leaf**



901

902 **Figure B2. Performance of random forest model RF2 on the test and Cross**  
903 **Validation (CV) sets according to the test metric by changing the hyperparameters:**  
904 **(a) N\_estimators (b) Max\_depth (c) Max\_features (d) Min\_samples\_leaf**



905

906 **Figure B3. Performance of random forest model RF3 on the test and Cross**  
907 **Validation (CV) sets according to the test metric by changing the hyperparameters:**  
908 **(a) N\_estimators (b) Max\_depth (c) Max\_features (d) Min\_samples\_leaf**

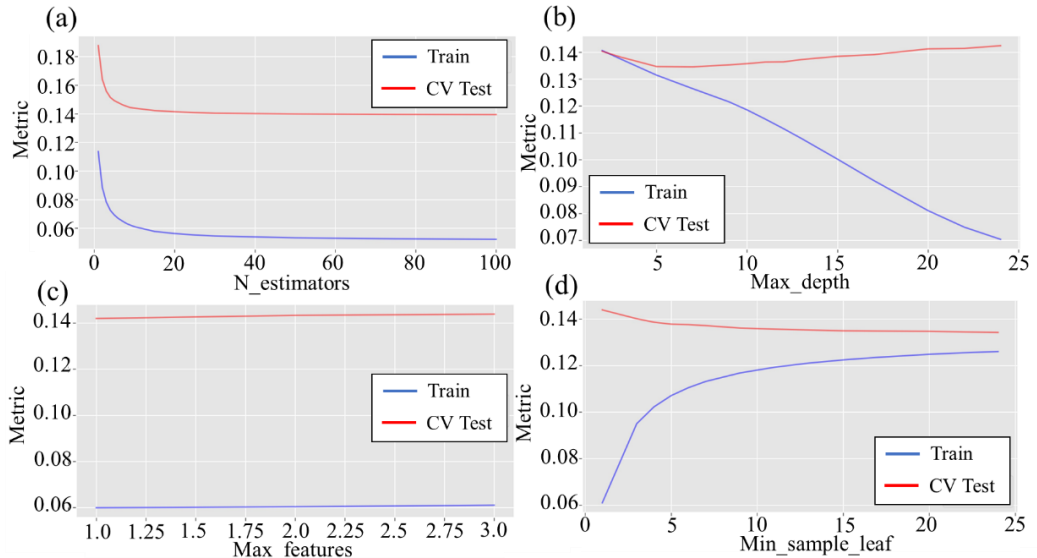


**Figure B4. Performance of random forest model RF4 on the test and Cross Validation (CV) sets according to the test metric by changing the hyperparameters:** (a) `N_estimators` (b) `Max_depth` (c) `Max_features` (d) `Min_samples_leaf`

The analysis of the previous figures provides the search grid of hyperparameters given in Table B1. After fitting each model K times (step 5), the optimal sets of hyperparameters are reported in Table B2 for each RF model. Then, the performance of models RF1, RF2, RF3, and RF4 are evaluated on the test dataset using RMSE metric. The obtained results are summarized in Table B3.

The above-described analysis has been used to identify the most informative triplet of variables, which has been chosen as the one corresponding to the best performing among the optimal RF models, namely RF2.

**Table B1. Hyperparameters range of variation**

Hyperparameter	Range of variation
<code>n_estimators</code>	5,10,20,25,30
<code>max_features</code>	1,2,3
<code>min_samples_leaf</code>	15,20,25
<code>max_depth</code>	3,4, 5, 6,7

924 **Table B2. Optimal values of Hyperparameters**

<b>Hyperparameter</b>	<b>Optimal values</b>			
	<b>RF1</b>	<b>RF2</b>	<b>RF3</b>	<b>RF4</b>
n_estimators	30	30	25	30
max_features	2	2	3	2
min_samples_leaf	20	20	9	20
max_depth	7	7	7	7

925

926 **Table B3. RMSE of studied models computed for the test dataset**

<b>Model</b>	<b>RMSE</b>
RF1 $\langle H, \theta_6, h_a \rangle$	0.122
RF2 $\langle H, \theta_{100}, h_a \rangle$	0.120
RF3 $\langle H, \theta_6, \theta_{100} \rangle$	0.140
RF4 $\langle \theta_6, \theta_{100}, h_a \rangle$	0.124

927

928

929

930 **Author contributions**

931 RG and DR formulated the research aim; PM provided the field measurements;  
932 PM and GS supplied the model simulations; DR and GS curated and analyzed  
933 the data; RG oversighted the research activities; DR worked on the preparation  
934 and the data visualization; DR, PM and GS wrote the draft manuscript; RG wrote  
935 the final version of the manuscript.

936 **Acknowledgements**

937 This research is part of the Ph.D. project entitled “Hydrological controls and  
938 geotechnical features affecting the triggering of shallow landslides in pyroclastic  
939 soil deposits” within the Doctoral Course “A.D.I.” of Università degli Studi della  
940 Campania “L. Vanvitelli”.

941 The research has been also funded by Università degli Studi della Campania ‘L.  
942 Vanvitelli’ through the programme “VALERE: VAnviteLli pEr la RicErca”.

943 **Competing interests**

944 At least one of the (co-)authors is a member of the editorial board of Hydrology  
945 and Earth System Sciences.

946 **References**

947 Allocca, V., Manna, F., and De Vita, P.: Estimating annual groundwater recharge  
948 coefficient for karst aquifers of the southern Apennines (Italy), Hydrol Earth Syst  
949 Sci, 18, 803–817, <https://doi.org/10.5194/hess-18-803-2014>, 2014.

950 Arthur, D. and Vassilvitskii, S.: k-means++: The Advantages of Careful Seeding,  
951 in: Proceedings of the Eighteenth Annual ACM-SIAM Symposium on Discrete  
952 Algorithms, 1027–1035, 2007.

953 Bogaard, T. A. and Greco, R.: Landslide hydrology: from hydrology to pore  
954 pressure, WIREs Water, 3, 439–459, <https://doi.org/10.1002/wat2.1126>, 2016.

- 955 Bogaard, T. A. and Greco, R.: Invited perspectives: Hydrological perspectives on  
956 precipitation intensity-duration thresholds for landslide initiation: proposing  
957 hydro-meteorological thresholds, *Nat. Haz. Earth Sys. Sci.*, 18, 31–39,  
958 <https://doi.org/10.5194/nhess-18-31-2018>, 2018.
- 959
- 960 Bordoni, M., Meisina, C., Valentino, R., Lu, N., Bittelli, M., and Chersich, S.:  
961 Hydrological factors affecting rainfall-induced shallow landslides: From the field  
962 monitoring to a simplified slope stability analysis, *Eng. Geol.*,  
963 <https://doi.org/10.1016/j.enggeo.2015.04.006>, 2015.
- 964 Breiman, L.: Random Forests, *Mach. Learn.*, 45, 5–32,  
965 <https://doi.org/https://doi.org/10.1023/A:1010933404324>, 2001.
- 966 Capretti, P. and Battisti, A.: Water stress and insect defoliation promote the  
967 colonization of *Quercus cerris* by the fungus *Biscogniauxia mediterranea*, *For.*  
968 *Pathol.*, 37, 129–135, <https://doi.org/10.1111/J.1439-0329.2007.00489.X>, 2007.
- 969 Cascini, L., Cuomo, S., and Guida, D.: Typical source areas of May 1998 flow-  
970 like mass movements in the Campania region, Southern Italy, *Eng. Geol.*, 96,  
971 107–125, <https://doi.org/10.1016/j.enggeo.2007.10.003>, 2008.
- 972 Cascini, L., Sorbino, G., Cuomo, S., and Ferlisi, S.: Seasonal effects of rainfall  
973 on the shallow pyroclastic deposits of the Campania region (southern Italy).  
974 *Landslides*, 11(5), 779–792. <https://doi.org/10.1007/s10346-013-0395-3>, 2014.
- 975 Celico, F., Naclerio, G., Bucci, A., Nerone, V., Capuano, P., Carcione, M.,  
976 Allocca, V., and Celico, P.: Influence of pyroclastic soil on epikarst formation:  
977 A test study in southern Italy, *Terra Nova*, 22, 110–115,  
978 <https://doi.org/10.1111/J.1365-3121.2009.00923.X>, 2010.
- 979 Chitu, Z., Bogaard, T. A., Busuioc, A., Burcea, S., Sandric, I., and Adler, M.-J.:  
980 Identifying hydrological pre-conditions and rainfall triggers of slope failures at

- 981 catchment scale for 2014 storm events in the Ialomita Subcarpathians, Romania,  
982 Landslides, 14, 419–434, <https://doi.org/10.1007/s10346-016-0740-4>, 2017.
- 983 Comegna, L., Damiano, E., Greco, R., Guida, A., Olivares, L., and Picarelli, L.:  
984 Field hydrological monitoring of a sloping shallow pyroclastic deposit, Can.  
985 Geotech. J., 53, 1125–1137, <https://doi.org/10.1139/cgj-2015-0344>, 2016.
- 986 Cowpertwait, P. S. P., O'Connell, P. E., Metcalfe, A. V., and Mawdsley, J. A.:  
987 Stochastic point process modelling of rainfall. I. Single-site fitting and validation,  
988 J. Hydrol., [https://doi.org/10.1016/S0022-1694\(96\)80004-7](https://doi.org/10.1016/S0022-1694(96)80004-7), 1996.
- 989 Dal Soglio, L., Danquigny, C., Mazzilli, N., Emblanch, C., and Massonnat, G.:  
990 Taking into Account both Explicit Conduits and the Unsaturated Zone in Karst  
991 Reservoir Hybrid Models: Impact on the Outlet Hydrograph. Water, 12, 3221,  
992 <https://doi.org/10.3390/w12113221>, 2020.
- 993 Damiano, E. and Olivares, L.: The role of infiltration processes in steep slope  
994 stability of pyroclastic granular soils: laboratory and numerical investigation,  
995 Nat. Haz., 52, 329–350, <https://doi.org/10.1007/s11069-009-9374-3>, 2010.
- 996 Damiano, E., Olivares, L., and Picarelli, L.: Steep-slope monitoring in  
997 unsaturated pyroclastic soils, Eng. Geol., 137–138, 1–12,  
998 <https://doi.org/10.1016/j.enggeo.2012.03.002>, 2012.
- 999 Damiano, E., Greco, R., Guida, A., Olivares, L., and Picarelli, L.: Investigation  
1000 on rainwater infiltration into layered shallow covers in pyroclastic soils and its  
1001 effect on slope stability, Eng. Geol., 220, 208–218,  
1002 <https://doi.org/10.1016/j.enggeo.2017.02.006>, 2017.
- 1003 de Amorim, R. C. and Hennig, C.: Recovering the number of clusters in data sets  
1004 with noise features using feature rescaling factors, Inf. Sci. (N Y), 324, 126–145,  
1005 <https://doi.org/10.1016/J.INS.2015.06.039>, 2015.

- 1006 De Vita, P., Agrello, D., and Ambrosino, F.: Landslide susceptibility assessment  
1007 in ash-fall pyroclastic deposits surrounding Mount Somma-Vesuvius:  
1008 Application of geophysical surveys for soil thickness mapping, *J. Appl.*  
1009 *Geophys.*, 59, 126–139, <https://doi.org/10.1016/j.jappgeo.2005.09.001>, 2006.
- 1010 Di Crescenzo, G. and Santo, A.: Debris slides—rapid earth flows in the carbonate  
1011 massifs of the Campania region (Southern Italy): morphological and  
1012 morphometric data for evaluating triggering susceptibility, *Geomorphology*, 66,  
1013 255–276, <https://doi.org/10.1016/j.geomorph.2004.09.015>, 2005.
- 1014 Efron, B. and Tibshirani, R.J., *An Introduction to the Bootstrap*. Chapman and  
1015 Hall, New York. <https://doi.org/10.1007/978-1-4899-4541-9>, 1993.
- 1016 Feddes, R. A., Kowalik, P., Kolinska-Malinka, K., and Zaradny, H.: Simulation  
1017 of field water uptake by plants using a soil water dependent root extraction  
1018 function, *J. Hydrol.*, 31, 13–26, [https://doi.org/10.1016/0022-1694\(76\)90017-2](https://doi.org/10.1016/0022-1694(76)90017-2),  
1019 1976.
- 1020 Fiorillo, F., Guadagno, F., Aquino, S., and De Blasio, A.: The December 1999  
1021 Cervinara landslides: Further debris flows in the pyroclastic deposits of  
1022 Campania (Southern Italy), *Bull. Eng. Geol. Env.*,  
1023 <https://doi.org/10.1007/s100640000093>, 2001.
- 1024 Forestieri, A., Caracciolo, D., Arnone, E., and Noto, L.V.: Derivation of Rainfall  
1025 Thresholds for Flash Flood Warning in a Sicilian Basin Using a Hydrological  
1026 Model, *Procedia Engineering*, 154, 818–825, ISSN 1877-7058,  
1027 <https://doi.org/10.1016/j.proeng.2016.07.413>, 2016.
- 1028 Gao, S. and Shain, L.: Effects of water stress on chestnut blight, *Can. J. For. Res.*,  
1029 25, 1030–1035, 1995.
- 1030 Greco, R. and Gargano, R.: A novel equation for determining the suction stress  
1031 of unsaturated soils from the water retention curve based on wetted surface area

- 1032 in pores, Water Resour Res, 51, 6143–6155,  
1033 <https://doi.org/10.1002/2014WR016541>, 2015.
- 1034 Greco, R., Comegna, L., Damiano, E., Guida, A., Olivares, L., and Picarelli, L.:  
1035 Hydrological modelling of a slope covered with shallow pyroclastic deposits  
1036 from field monitoring data, Hydrol. Earth. Syst. Sci., 17, 4001–4013,  
1037 <https://doi.org/10.5194/hess-17-4001-2013>, 2013.
- 1038 Greco, R., Comegna, L., Damiano, E., Guida, A., Olivares, L., and Picarelli, L.:  
1039 Conceptual Hydrological Modeling of the Soil-bedrock Interface at the Bottom  
1040 of the Pyroclastic Cover of Cervinara (Italy), Procedia Earth and Planetary  
1041 Science, <https://doi.org/10.1016/j.proeps.2014.06.007>, 2014.
- 1042 Greco, R., Marino, P., Santonastaso, G. F., and Damiano, E.: Interaction between  
1043 Perched Epikarst Aquifer and Unsaturated Soil Cover in the Initiation of Shallow  
1044 Landslides in Pyroclastic Soils, Water, 10, 948,  
1045 <https://doi.org/10.3390/w10070948>, 2018.
- 1046 Greco, R., Comegna, L., Damiano, E., Marino, P., Olivares, L., and Santonastaso,  
1047 G. F.: Recurrent rainfall-induced landslides on the slopes with pyroclastic cover  
1048 of Partenio Mountains (Campania, Italy): Comparison of 1999 and 2019 events,  
1049 Eng Geol, 288, 106160, <https://doi.org/10.1016/j.enggeo.2021.106160>, 2021.
- 1050 Greco, R., Marino, P., and Bogaard, T. A.: Recent Advancements of Landslide  
1051 Hydrology, WIREs Water, e1675. <https://doi.org/10.1002/wat2.1675>, 2023.
- 1052 Hartmann, A., Goldscheider, N., Wagener, T., Lange, J., and Weiler, M.: Karst  
1053 water resources in a changing world: Review of hydrological modeling  
1054 approaches, Reviews of Geophysics, 52, 218–242,  
1055 <https://doi.org/10.1002/2013RG000443>, 2014.

- 1056 Herman, J., and Usher, W.: SALib: an open-source Python library for Sensitivity  
1057 Analysis. *The Journal of Open Source Software*, 2(9), 97,  
1058 <https://doi.org/10.21105/joss.00097>, 2017.
- 1059 Iwanaga, T., Usher, W., and Herman, J.: Toward SALib 2.0: Advancing the  
1060 accessibility and interpretability of global sensitivity analyses. *Socio-*  
1061 *Environmental Systems Modelling*, 4, 18155–18155,  
1062 <https://doi.org/10.18174/SESMO.18155>, 2022.
- 1063 Lloyd, S. P.: Least Squares Quantization in PCM, *IEEE Trans. Inf. Theory*, 28,  
1064 1982.
- 1065 Lu, N. and Likos, W. J.: Suction Stress Characteristic Curve for Unsaturated Soil,  
1066 *J. Geotech. Geoenv. Eng.*, [https://doi.org/10.1061/\(asce\)1090-0241\(2006\)132:2\(131\)](https://doi.org/10.1061/(asce)1090-0241(2006)132:2(131)), 2006.
- 1068 Marino, P., Comegna, L., Damiano, E., Olivares, L., and Greco, R.: Monitoring  
1069 the Hydrological Balance of a Landslide-Prone Slope Covered by Pyroclastic  
1070 Deposits over Limestone Fractured Bedrock, *Water*, 12, 3309,  
1071 <https://doi.org/10.3390/w12123309>, 2020a.
- 1072 Marino, P., Peres, D.J., Cancelliere, A., Greco, R. and Bogaard, T. A.: Soil  
1073 moisture information can improve shallow landslide forecasting using the  
1074 hydrometeorological threshold approach, *Landslides* 17, 2041–2054,  
1075 <https://doi.org/10.1007/s10346-020-01420-8>, 2020b.
- 1076 Marino, P., Santonastaso, G. F., Fan, X., and Greco, R.: Prediction of shallow  
1077 landslides in pyroclastic-covered slopes by coupled modeling of unsaturated and  
1078 saturated groundwater flow, *Landslides*, <https://doi.org/10.1007/s10346-020-01484-6>, 2021.
- 1080 McDowell, N., Pockman, W. T., Allen, C. D., Breshears, D. D., Cobb, N., Kolb,  
1081 T., Plaut, J., Sperry, J., West, A., Williams, D. G., and Yepez, E. A.: Mechanisms

- 1082 of plant survival and mortality during drought: Why do some plants survive while  
1083 others succumb to drought?, *New Phytologist*, 178, 719–739,  
1084 <https://doi.org/10.1111/J.1469-8137.2008.02436.X>, 2008.
- 1085 Nieber, J. L. and Sidle, R. C.: How do disconnected macropores in sloping soils  
1086 facilitate preferential flow?, *Hydrol. Process.*, 24, 1582–1594,  
1087 <https://doi.org/10.1002/hyp.7633>, 2010.
- 1088 Olivares, L. and Picarelli, L.: Shallow flowslides triggered by intense rainfalls on  
1089 natural slopes covered by loose unsaturated pyroclastic soils, *Geotechnique*,  
1090 <https://doi.org/10.1680/geot.2003.53.2.283>, 2003.
- 1091 Pagano, L., Picarelli, L., Rianna, G., and Urciuoli, G.: A simple numerical  
1092 procedure for timely prediction of precipitation-induced landslides in unsaturated  
1093 pyroclastic soils, *Landslides*, 7, 273–289, <https://doi.org/10.1007/s10346-010-0216-x>, 2010.
- 1095 Pan, S., Pan, N., Tian, H., Friedlingstein, P., Sitch, S., Shi, H., Arora, V. K.,  
1096 Haverd, V., Jain, A. K., Kato, E., Lienert, S., Lombardozzi, D., Nabel, J. E. M.  
1097 S., Ottlé, C., Poulter, B., Zaehle, S., and Running, S. W.: Evaluation of global  
1098 terrestrial evapotranspiration using state-of-the-art approaches in remote sensing,  
1099 machine learning and land surface modeling, *Hydrol. Earth. Syst. Sci.*, 24, 1485–  
1100 1509, <https://doi.org/10.5194/hess-24-1485-2020>, 2020.
- 1101 Paulik, C., Dorigo, W., Wagner, W., and Kidd, R.: Validation of the ASCAT Soil  
1102 Water Index using in situ data from the International Soil Moisture Network, *Int.*  
1103 *J. Appl. Earth Obs.* . *Geoinf.*, 30, 1–8,  
1104 <https://doi.org/10.1016/J.JAG.2014.01.007>, 2014.
- 1105 Pedregosa, F., Varoquaux, G., Gramfort, A., Michel, V., Thirion, B., Grisel, O.,  
1106 Blondel, M. Prettenhofer, P., Weiss, R., Dubourg, V., Vanderplas, J., Passos, A.,

- 1107 Cournapeau, D., Brucher, M., Perrot, M., and Duchesnay, E.: Scikit-learn:  
1108 Machine Learning in Python. *J. Mach. Lear. Res.*, 12, 2825–2830, 2011.
- 1109 Peres, D. J. and Cancelliere, A.: Derivation and evaluation of landslide-triggering  
1110 thresholds by a Monte Carlo approach, *Hydrol. Earth Syst. Sci.*, 18, 4913–4931,  
1111 <https://doi.org/10.5194/hess-18-4913-2014>, 2014.
- 1112 Peres, D. J., Cancelliere, A., Greco, R., and Bogaard, T. A.: Influence of uncertain  
1113 identification of triggering rainfall on the assessment of landslide early warning  
1114 thresholds, *Nat. Hazards Earth Syst. Sci.*, 18, 633–646,  
1115 <https://doi.org/10.5194/nhess-18-633-2018>, 2018.
- 1116 Perrin, J., Jeannin, P. Y., and Zwahlen, F.: Epikarst storage in a karst aquifer: A  
1117 conceptual model based on isotopic data, Milandre test site, Switzerland. *J.*  
1118 *Hydrol.*, 279(1-4), 106-124, [https://doi.org/10.1016/S0022-1694\(03\)00171-9](https://doi.org/10.1016/S0022-1694(03)00171-9),  
1119 2003.
- 1120 Pirone, M., Papa, R., Nicotera, M. V., and Urciuoli, G.: Soil water balance in an  
1121 unsaturated pyroclastic slope for evaluation of soil hydraulic behaviour and  
1122 boundary conditions, *J. Hydrol.*, <https://doi.org/10.1016/j.jhydrol.2015.06.005>,  
1123 2015.
- 1124 Ponce, V. M. and Hawkins, R. H.: Runoff Curve Number: Has It Reached  
1125 Maturity?, *J. Hydrol. Eng.*, 1, 11–19, [https://doi.org/10.1061/\(ASCE\)1084-0699\(1996\)1:1\(11\)](https://doi.org/10.1061/(ASCE)1084-0699(1996)1:1(11)), 1996.
- 1127 Revellino, P., Guerriero, L., Gerardo, G., Hungr, O., Fiorillo, F., Esposito, L.,  
1128 and Guadagno, F. M.: Initiation and propagation of the 2005 debris avalanche at  
1129 Nocera Inferiore (Southern Italy), *Ital. J. Geosci.*,  
1130 <https://doi.org/10.3301/IJG.2013.02>, 2013.
- 1131 Reichenbach, P., Cardinali, M., De Vita, P., and Guzzetti, F.: Regional  
1132 hydrological thresholds for landslides and floods in the Tiber River Basin (central

- 1133 Italy), Environ. Geol., 35, 146–159, <https://doi.org/10.1007/s002540050301>,  
1134 1998.
- 1135 Richards, L. A.: Capillary conduction of liquids through porous mediums, J.  
1136 Appl. Phys., <https://doi.org/10.1063/1.1745010>, 1931.
- 1137 Rodriguez-Iturbe, I., Febres De Power, B., and Valdes, J. B.: Rectangular pulses  
1138 point process models for rainfall: analysis of empirical data, J. Geophys. Res.,  
1139 <https://doi.org/10.1029/JD092iD08p09645>, 1987.
- 1140 Rolandi, G., Bellucci, F., Heizler, M. T., Belkin, H. E., and De Vivo, B.: Tectonic  
1141 controls on the genesis of ignimbrites from the Campanian Volcanic Zone,  
1142 southern Italy, Miner. Petrol., 79, 3–31, <https://doi.org/10.1007/s00710-003-0014-4>, 2003.
- 1144 Rousseeuw, P. J.: Silhouettes: A graphical aid to the interpretation and validation  
1145 of cluster analysis, J. Comput. Appl. Math., 20, 53–65,  
1146 [https://doi.org/10.1016/0377-0427\(87\)90125-7](https://doi.org/10.1016/0377-0427(87)90125-7), 1987.
- 1147 Saltelli, A.: Making best use of model evaluations to compute sensitivity indices.  
1148 Computer Physics Communications, 145(2), 280–297,  
1149 [https://doi.org/10.1016/S0010-4655\(02\)00280-1](https://doi.org/10.1016/S0010-4655(02)00280-1), 2002.
- 1150 Segoni, S., Piciullo, L. and Gariano, S.L.: A review of the recent literature on  
1151 rainfall thresholds for landslide occurrence, Landslides, 15, 1483–1501,  
1152 <https://doi.org/10.1007/s10346-018-0966-4>, 2018.
- 1153 Shuttleworth, W. J.: Evaporation, in: Handbook of Hydrology, edited by:  
1154 Maidment, D. R., McGraw-Hill, New York, NY, USA, 1993.
- 1155 Sobol, I. M.: Global sensitivity indices for nonlinear mathematical models and  
1156 their Monte Carlo estimates. Mathematics and Computers in Simulation, 55(1–  
1157 3), 271–280, [https://doi.org/10.1016/S0378-4754\(00\)00270-6](https://doi.org/10.1016/S0378-4754(00)00270-6), 2001.

- 1158 Stone M.: Cross-validatory choice and assessment of statistical predictions. J.  
1159 Royal Stat. Soc., 36(2), 111–147, 1974.
- 1160 Tromp-Van Meerveld, H. J. and McDonnell, J. J.: Threshold relations in  
1161 subsurface stormflow: 1. A 147-storm analysis of the Panola hillslope, Water  
1162 Resour. Res., 42, 2410, <https://doi.org/10.1029/2004WR003778>, 2006a.
- 1163 Tromp-Van Meerveld, H. J. and McDonnell, J. J.: Threshold relations in  
1164 subsurface stormflow: 2. The fill and spill hypothesis, Water Resour. Res.,  
1165 <https://doi.org/10.1029/2004WR003800>, 2006b.
- 1166 Tufano, R., Formetta, G., Calcaterra, D., and De Vita, P.: Hydrological control  
1167 of soil thickness spatial variability on the initiation of rainfall-induced shallow  
1168 landslides using a three-dimensional model, Landslides, 18, 3367-3380,  
1169 <https://doi.org/10.1007/s10346-021-01681-x>, 2021.
- 1170 Twarakavi, N. K. C., Sakai, M., and Šimůnek, J.: An objective analysis of the  
1171 dynamic nature of field capacity, Water Resour. Res., 45,  
1172 <https://doi.org/10.1029/2009WR007944>, 2009.
- 1173 van Genuchten, M. Th.: A Closed-form Equation for Predicting the Hydraulic  
1174 Conductivity of Unsaturated Soils1, Soil Sci. Soc. Am. J., 44, 892,  
1175 <https://doi.org/10.2136/sssaj1980.03615995004400050002x>, 1980.
- 1176 Wicki, A., Lehmann, P., Hauck, C., Seneviratne, S. I., Waldner, P., and Stähli,  
1177 M.: Assessing the potential of soil moisture measurements for regional landslide  
1178 early warning, Landslides, 17, 1881–1896, <https://doi.org/10.1007/S10346-020-01400-Y>, 2020.
- 1180 Williams, P. W.: The role of the epikarst in karst and cave hydrogeology: a  
1181 review, Int. J. Speleol., 37, 1–10, <https://doi.org/10.5038/1827-806X.37.1.1>,  
1182 2008.
- 1183